University of Padova

School of Engineering

Master's Level Degree in Bioengineering

Developing multi-modal analysis of brain anatomical connectivity using quantitative MRI data

Candidate

Emma Biondetti

First supervisor

Prof.ssa Alessandra Bertoldo

Second supervisor

Dr. Claudia A.M. Wheeler-Kingshott

Academic Year 2013/2014

Abstract

The aim of this work is to develop a method to investigate connectivity properties of a specific set of Grey Matter regions in the brain, and its relationship with connectivity described by the fibre structure of underlying White Matter. Data were acquired with Magnetic Resonance Imaging, a flexible, widely available, non-invasive imaging technique, which can picture in vivo the *connectome*, a comprehensive map of neural connections in the living brain. We worked with scans of healthy subjects and patients affected by Secondary-Progressive Multiple Sclerosis.
In Chapter 1 we introduce the imaging technique, the gross anatomy of the brain and a description of the MS disease. In Chapter 2 we present the method we started from that used Grey Matter cortical thickness to establish connectivity matrix of the brain. We then describe the development that we performed to extend the study to combine connectivity using cortical thickness with that obtained investigating White Matter fibre tractography. We assess the developed method of investigation using only the data from controls. In Chapter 3 we describe the results of the study performed on both the groups of subjects and we comment the outcome.
With this work, we calculated two connectivity networks for each group of subjects: one described interconnectivity of a relevant set of Grey Matter areas, chosen according to the Principal Network technique [1]; the other described connections between a specific set of sub-cortical White Matter regions based on the Grey Matter connectivity analysis, and it was investigated with Diffusion Tensor Imaging and probabilistic tractography. By studying the global efficiency of these networks, obtained for Grey and White Matter structures belonging to the same anatomical regions, we characterized the difference between controls and patients, showing that the efficiency always resulted to be impaired in the second group. Then, by studying the statistical differentiation of cortical thickness values between patients and controls, we investigated the possible causes of differentiation of connectivity in the Grey Matter between the two groups. Similarly, by considering the distributions of values of Fractional Anisotropy in controls and patients, we analyzed the differentiation of connectivity in the White Matter. Finally, we compared the patterns of the connectivity metrics obtained from cortical thickness of Grey Matter regions and White Matter tractography in order to test the correlation between the measures of connectivity showed in this dissertation.

Contents

List of Figures

List of Tables

List of Acronyms

AC anterior commissure

PC posterior commissure

BET Brain Extraction Tool

CC Clustering Coefficient

CNS Central Nervous System

CSD Constrained Spherical Deconvolution

CSF CerebroSpinal Fluid

DMN Default Mode Network

DT Diffusion Tensor

DTI Diffusion Tensor Imaging

DW Diffusion weighted

Eg Global Efficiency

El Local Efficiency

EPI Echo Planar Imaging

FA Fractional Anisotropy

FAST FMRIB's Automated Segmentation Tool

FFE Fast Field Echo

FID Free Induction Decay

FLIRT FMRIB's Linear Image Registration Tool

dODF diffusion Orientation Density Function

fODF fibre Orientation Density Function

FSL FMRIB Software Library

GCA Gaussian Classifier Atlas

GM Grey Matter

GUI Graphical User Interface

HARDI High Angular Resolution Diffusion Imaging

ICBM International Consortium for Brain Mapping

MD Mean Diffusivity

MR Magnetic Resonance

MRI Magnetic Resonance Imaging

MS Multiple Sclerosis

NRES National Research Ethics Service

NIfTI Neuroimaging Informatics Technology Initiative

NMR Nuclear Magnetic Resonance

ODF Orientation Density Function

PCA Principal Component Analysis

PDF Probability Distribution Function

PN Principal Network

PP Primary-Progressive

PR Progressive-Relapsing

QQ Quantile-Quantile

RF Radio-Frequency

RH Rotational Harmonic

ROI Region Of Interest

RR Relapsing-Remitting

SE Spin Echo

SENSE Sensitivity Encoding

SH Spherical Harmonic

SNR Signal-to-Noise Ratio

SP Secondary-Progressive

T1-w T1-weighted

T2-w T2-weighted

UCL University College of London

WM White Matter

Chapter 1

Introduction

This chapter is an introduction to the theoretical aspects of the dissertation. In Section 1.1 we present the imaging technique used to acquire our data set [2, 3]. In Section 1.2 we describe the gross anatomy of brain and the field of study of connectomics. Finally, in Section 1.3 we outline the clinical context of our work.

1.1 Magnetic Resonance Imaging

Magnetic Resonance Imaging (MRI) is a technique able to image soft tissues and metabolic processes therein. It is widely appreciated because of its flexibility and sensitivity to a broad range of tissue properties, and for its relative safety, because of the non-invasive nature of the magnetic fields employed.
MRI originated from the application of Nuclear Magnetic Resonance (NMR) to radiological imaging. The adjective *magnetic* refers to the use of magnetic fields, while *resonance* refers to the need to match the Radio-Frequency (RF) of an oscillating magnetic field to the precessional frequency of the spin of a *nucleus* in a tissue molecule. The dominant nucleus in MRI is the proton of hydrogen: imaging of humans is based on the manipulation of hydrogen spins precession with a combination of magnetic fields, and on its subsequent detection in organic molecules.
MRI produces NMR images of a slice through the human body. Each slice has a *thickness* and is composed of several volume elements called *voxels*. The MRI image is composed of several picture elements, the *pixels*. The intensity of a pixel is proportional to the NMR signal intensity of the content of the corresponding voxel of the object being imaged.
As a reference for future discussion, in Figure 1.1 we show the coordinate system

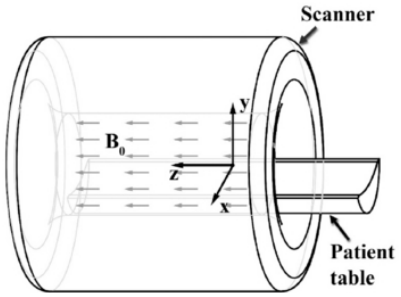

Figure 1.1: MRI coordinate system

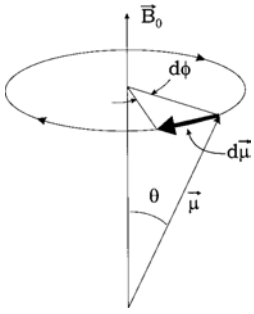

Figure 1.2: Proton spin precession about the external magnetic field

used in MRI. The z axis is parallel to the external magnetic field $\overrightarrow{B}_0$, and is called *longitudinal direction*. The $x - y$ plane perpendicular to the longitudinal direction is the *transverse plane*.
In Subsection 1.1.1 we provide an overview of the basic physics principles involved, then in Subsection 1.1.2 and Subsection 1.1.3 we introduce some modalities of structural images acquisition and some of the most common artifacts in MRI.

1.1.1 Physics principles

Fundamental interaction of proton spin and magnetic field

We define as *precession* the circular motion of the axis of rotation of a spinning body about another fixed axis, caused by the application of a torque in the direction of precession.
The interaction of the proton of hydrogen spin with an external magnetic field $\overrightarrow{B}_0$ produces a torque, causing the spin to precess about the $\overrightarrow{B}_0$ field direction (Figure 1.2). The proton spin can be thought of as leading to a circulating electric current, and, hence, an associated magnetic moment. The direct relationship between the magnetic moment $\overrightarrow{\mu}$ and the spin angular momentum $\overrightarrow{J}$ is found by experiment:

$$\overrightarrow{\mu} = \gamma \overrightarrow{J} \tag{1.1}$$

γ is a constant called gyromagnetic ratio[1]. From (1.1) we are justified, in any discussion, to refer either to spin, or to the magnetic dipole moment, since they track each other.
The precession of the proton magnetic moment vector is clockwise and given by the Larmor equation:

$$\omega_0 = \gamma B_0 \tag{1.2}$$

where γ is the gyromagnetic ratio and ω_0 is called Larmor frequency.

Equilibrium alignment of spins

The presence of an external static magnetic field leads to splittings of the atomic or nuclear energy levels of atomic or nuclear magnetic moments (*Zeeman effect*). In

[1] in water the proton of hydrogen has $\gamma = 2.68 \times 10^8$ rad/s/T

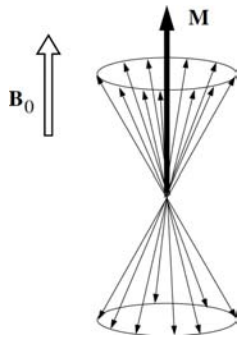

Figure 1.3: Macroscopic magnetization vector

the case of the proton of hydrogen, the quantization of the magnetic moment (1.1) gives two discrete energy values:

$$E = -\overrightarrow{\mu} \cdot \overrightarrow{B} = -\mu_z B_z = -\gamma m_s \hbar B_z \tag{1.3}$$

with

$$m_s = \pm\frac{1}{2}$$

From (1.3) a spin in the presence of a constant field $\overrightarrow{B} = B_0\hat{z}$ has only two possible alignments: parallel to the field (low-energy) and anti-parallel (high-energy).
The magnitude of energy absorbed or released by the proton spin system, upon a transition between the two energy states, is found from (1.3):

$$\Delta E = E\left(m_s = -\frac{1}{2}\right) - E\left(m_s = \frac{1}{2}\right) = \frac{1}{2}\gamma\hbar B_0 - (\frac{1}{2}\gamma\hbar B_0) = \hbar\omega_0 \tag{1.4}$$

Significantly, the frequency in (1.4) is the Larmor precession frequency (1.2).

Macroscopic magnetization

In presence of $\overrightarrow{B}_0$, ^{1}H spins align to one of the two possible directions according to Boltzmann's statistics:

$$\frac{N_{up}}{N_{down}} = \exp\frac{\Delta E}{kT} \tag{1.5}$$

where k is the Boltzmann's constant and T is the absolute temperature, and kT is the average thermal energy. At human body temperature, the quantum spin energy is extremely small if compared to the thermal energy, giving $\Delta E \ll kT$ and

$$\exp\frac{\Delta E}{kT} \approx 1 + \exp\frac{\Delta E}{kT} = 1 + \frac{\gamma\hbar B_0}{kT}$$

$$\frac{N_{up}}{N_{down}} - 1 = \frac{\gamma\hbar B_0}{kT}$$

$$\frac{N_{up} - N_{down}}{N_s} \approx \frac{\gamma\hbar B_0}{2kT} \tag{1.6}$$

where $N_s = N_{up} + N_{down}$ is the total number of spins. At a temperature of T = 300K and magnetic field $B_0 = 1$T the number of protons that can be activated to generate a NMR signal (1.6) is $\approx 3 \times 10^{-6}$. This is a very low value, so it might be guessed

(a) Rotating reference frame **(b)** Fixed reference frame

Figure 1.4: Effect of RF pulse application

that no significant signal is detectable at human body temperature. However, there are Avogadro number of protons in a few grams of tissue.
At a given temperature N_{up} and N_{down} are constant in time, but in dynamic equilibrium. We consider the *macroscopic magnetization* (Figure 1.3) as the vector sum of the spins magnetic moments

$$\overrightarrow{M} = \sum_i \overrightarrow{\mu}_i \tag{1.7}$$

The equilibrium value of (1.7) along the external field direction is the *longitudinal equilibrium magnetization* M_0. If we consider a sample with spin density ρ_0, M_0 is given by the proton magnetic moment component $\gamma\hbar/2$ multiplied by the relative spin excess times the spin density:

$$M_0 = \frac{\rho_0 \gamma \hbar^2 \omega_0}{4kT}$$

Noting (1.2), we have:

$$M_0 = \frac{\rho_0 \gamma^2 \hbar^2}{4kT} B_0 \tag{1.8}$$

This equilibrium value, while limited by the spin excess, leads to a measurable NMR effect.

NMR signal

In presence of the static magnetic field, a perturbation is applied to the system for a time $\Delta t = \tau_p$ and the recovering condition is observed. The perturbation is obtained by applying of a low intensity ($\approx \mu$T) magnetic field $\overrightarrow{B}_1$ perpendicular to $\overrightarrow{B}_0$. $\overrightarrow{B}_1$ rotates about $\overrightarrow{B}_0$ in the $x-y$ plane and is applied for a short time (≈ms). If the frequency ω_{rf} of $\overrightarrow{B}_1$ equals the Larmor frequency ω_0, we obtain a resonance effect. The energy that a spin in order to requires to change its energy state is the same energy provided by a pulse in the RF range.
$\overrightarrow{B}_1$ is applied by a transmit coil tuned to the Larmor frequency:

- in a frame rotating with $\overrightarrow{B}_1$, $\overrightarrow{M}$ precesses about the x_1 axis, with an angular speed ω_1, and *flip angle* $\alpha = \omega_1 \tau$ (Figure 1.4a);
- in a fixed frame, causes $\overrightarrow{M}$ spirally rotates about $\overrightarrow{B}_0$ with angular speed Ω_0 (Figure 1.4b).

(a) Receive coil in the $x-y$ plane **(b)** FID

Figure 1.5: FID measurement

The application of a $\pi/2$-RF pulse places the $\overrightarrow{M}$ vector in the $x-y$ plane. This results in the disappearance of the longitudinal component M_z, and in the appearance of a transverse component M_{xy}. After the pulse application, the equilibrium condition is restored through an exponential recover of M_z and an exponential decay of M_{xy}:

$$M_z \propto 1 - \exp \frac{t}{T_1} \quad M_{xy} \propto \exp -\frac{t}{T_2}$$

The time-varying transverse magnetization M_{xy} produces a time-varying magnetic flux. This flux induces a voltage in a receive coil (Figure 1.5a), according to the Faraday-Lenz law:

$$V \propto -\frac{\partial \Phi}{\partial t} \tag{1.9}$$

The NMR signal is the Free Induction Decay (FID), a sinusoidal signal of frequency $f = \omega_0/(2\pi)$ and amplitude that decreases with $\tau = T_2$ (Figure 1.5b).

Relaxation times

FID is influenced by three important factors: the interactions of the spins with their surroundings, the dephasing of clusters of spins and the magnetic field inhomogeneities.
The first factor, called *spin-lattice* decay, is responsible for the recovering of the initial longitudinal magnetization M_z. The rate of regrowth is characterized by a constant T_1 called the *longitudinal relaxation time* and arises from the interactions between the spins and the atomic neighbourhood. The magnetization time evolution is described by the solutions for the Bloch equations which incorporate both relaxation and precession effects. The description of how M_z recovers its initial magnetization M_0 is given by

$$M_z(t) = M_z(0)(1 - e^{-t/T_1}) \tag{1.10}$$

The second factor, called *spin-spin* decay, is caused by the variations in the local precessional frequencies. It is characterized by the time constant T_2 that describes the rate at which the transverse component M_{xy} decays. The equation governing this behaviour is

$$M_{xy}(t) = M_0 e^{-t/T_2} \tag{1.11}$$

Actually, there are two factors that contribute to the decay of the transverse magnetization: the spin-spin interactions, that give a pure T_2 molecular effect, and the

variations of the external magnetic field B_0, that lead to an inhomogeneous T_2 effect. The combined time constant is given by the symbol T_2^*:

$$\frac{1}{T_2^*} = \frac{1}{T_2} + \gamma \Delta B \tag{1.12}$$

with $\Delta B = 0$ if B_0 is homogeneous. Thus the signal picked up by the receiver is described by the following equation:

$$M_{xy}(t) = M_0 e^{-t/T_2^*} \cos \omega_0 t \tag{1.13}$$

Resolution and contrast

Spatial resolution in MRI does not depend upon the wavelength of the input RF field. RF generally have wavelengths of the order of meters, yet the resolution in MRI is on the order of millimeters. In fact, the inherent resolution in MRI is a function of the way the signal and noise are sampled and filtered, and it is ultimately limited only by the diffusion of the protons through the tissue and the local magnetic field non-uniformities around the proton.
MRI is versatile because of its sensitivity to a large set of variables, that permits images to be generated with different levels of contrast based upon the desired usage. The three main tissue parameters of influence are the spin density and the two relaxation times T_1 and T_2. The visualization of their effect can be enhanced and controlled by setting two values: T_R and T_E. T_R is the *repetition time*, the time interval that occurs between the application of two subsequent RF pulses. T_E is the *echo time*, the time lapse between the application of the RF pulse and the measurement of the signal.
Examining the behaviour of the exponentials in (1.10) and (1.11), we observe that:

- for long T_R and short T_E the image is sensitive only to the tissue spin density (Figure 1.6a);
- for $T_E \simeq T_2$ and long T_R, the image is weighted both by spin density and T_2 and the contrast between different T_2 is enhanced (Figure 1.6b);
- for $T_R \leq T_1$ and short T_E, the image is weighted by both spin density and T_1 (Figure 1.6c).

These three different acquisitions create different contrasts between White Matter (WM), Grey Matter (GM) and CerebroSpinal Fluid (CSF).

Frequency encoding and image reconstruction

The goal of MRI is to correlate a series of signal measurements with the spatial locations of the various sources. When all the protons are represented by just one chemical species such as water and the static magnetic field is uniform, then the signal is generated from all the spins, regardless their position in the magnetic field. For this reason we must introduce a *gradient*, a spatially changing magnetic field across the sample to produce signal with spatially varying frequency components. As an example, a linear gradient applied along the x direction gives:

$$B(x) = B_0 + G_x x$$

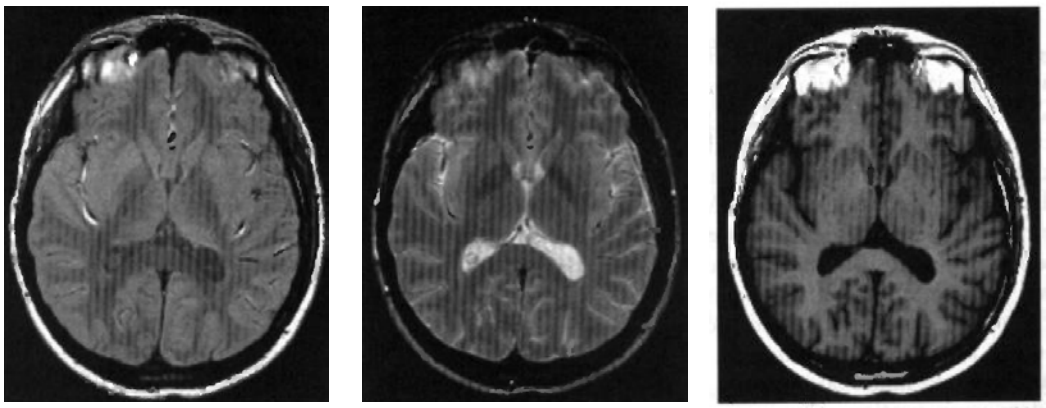

(a) Spin density-weighted **(b)** T_2-weighted **(c)** T_1-weighted

Figure 1.6: Three different kinds of contrast in MRI scans of the head

And according to (1.2):

$$\Omega = \gamma B_0 \Rightarrow \gamma B(x) = \gamma B_0 + \gamma G_x x$$

thus we can relate the spatial component to the frequency $f = \Omega/(2\pi)$:

$$x = \frac{\Omega/\gamma - B_0}{G_x} = g(\Omega)$$

This means that the spectral components now represent spatial information, and, in turn, leads to the possibility that the signal could be inverted and the physical object could be reconstructed, or imaged.
The mapping back and forth between signal space and the image position space may be carried out with a Fourier transform. With more gradient coils, data reconstruction by inverse Fourier transform can be carried out in more spatial dimensions, realizing two and three dimensional imaging.

Fourier method This method is based on phase and frequency encoding. Encoding procedure consists of three steps: preparation, phase encoding of the first coordinate and frequency encoding of the second coordinate.

1. In the preparation step a gradient G_z is applied along the z axis to select the axial section

   $$\Omega(z) = \gamma(B_0 + G_z z) = \Omega_0 + \gamma G_z z \tag{1.14}$$

   then a $(\pi/2)$-RF pulse is applied, with $f^* = \Omega^*/(2\pi)$

   $$\Omega^* = \Omega(z_p) = \Omega_0 + \gamma_z z_p$$

   in this way, only spins at $z = z_p$ are set into precession.
   From (1.14) in order to have a good resolution in the z direction, a narrow bandwidth pulse is required. As shown in Figure 1.7, slice position depends upon the bandwidth centre frequency, slice thickness depends upon bandwidth and gradient values.

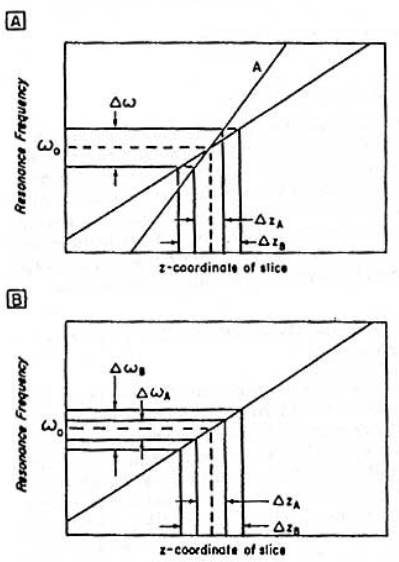

Figure 1.7: Slice position and thickness

2. A gradient G_y is applied to phase encode the y coordinate in the section:

$$\Omega(y) = \Omega_0 + \gamma G_y y$$

After an application time of length t_y, all the spins at the same y coordinate have equal phase:

$$\phi_y = (\Omega_0 + \gamma G_y y)t_y$$

3. A reading gradient G_x is applied to frequency encode the x coordinate in the section:

$$\Omega(x) = \Omega_0 + \gamma G_x x$$

all the spins at the same x coordinate have equal frequency $\Omega(x)/2\pi$. Thus, every point in the $x - y$ plane is uniquely identified by the pair (Ω_x, ϕ_y).

The FID signal received from the voxel at coordinates (x, y) is

$$I(x, y) \exp j(\Omega t + \phi)$$

where $I(x, y)$ is function of $M_{xy}(T_1, T_2, \rho)$. With a Ω_r demodulation, the frequency shift leads to

$$I(x, y) \exp j((\Omega - \Omega_r)t + \phi)$$

By applying the Fourier encoding method, the contribution of the voxel (x, y) to the total signal is

$$S_{x,y}(t) = I(x, y) \exp j((\Omega_x - \Omega_r)t + \phi_y)$$

After the replacement of the encoded coordinates values and the extension of the formula to the entire slice, we have the total signal (we ignore the contribution of the constant value $\Omega_0 t$):

$$S(t) = \int_{-\infty}^{+\infty} \int_{-\infty}^{+\infty} I(x, y) \exp j[(\Omega_0 - \Omega_r)t + \gamma G_x x t + \gamma G_y y t_y] dx dy$$

With

$$\Omega = \Omega_r \quad k_x = \frac{\gamma G_x t_x}{2\pi} \quad k_y = \frac{\gamma G_x t_x}{2\pi}$$

and $t = t_x$ the time at which the FID is sampled, we have

$$S(t)|_{t=t_x} = \int_{-\infty}^{+\infty} \int_{-\infty}^{+\infty} I(x,y) \exp j[(\Omega_0 - \Omega_r)t + \gamma G_x x t_x + \gamma G_y y t_y] dxdy$$

and

$$s(k_x, k_y) = \int_{-\infty}^{+\infty} \int_{-\infty}^{+\infty} I(x,y) \exp j2\pi[k_x x + k_y y] dxdy \tag{1.15}$$

where $s(k_x, k_y)$ is called *k-space*. As a result, $I(x,y)$ is obtained through the Fourier transform of (1.15).
Basically, N FID signals are acquired by applying an increasing value of G_y, and each FID is sampled N times by increasing the value of t_x. The results are organized in a $N \times N$ matrix of $s(k_x, k_y)$ values, and $I(x,y)$ is obtained from the matrix using the discrete Fourier transform.

Magnetic field strength

MRI scanners (Figure 1.8) can be subdivided into five categories based on B_0 strength:

- ultrahigh field (4T - 7T);
- high field (1.5T - 3T);
- midfield (0.5T - 1.4T);
- low field (0.2T - 0.4T);
- ultralow field (<0.2T)

The interest in high and ultrahigh magnetic fields for clinical application and research stems from the fact that the Signal-to-Noise Ratio (SNR) increases with field strength. The signal exhibits quadratic growth with B_0, though this is partially offset by the fact that the noise starts to have linear B_0 dependence at high fields.

1.1.2 Structural MRI

We refer to structural MRI as to the set of techniques providing static anatomical information. Complementary information is provided by functional MRI, a group of techniques giving insight into dynamic physiological processes. In this work we will only refer to structural acquisition techniques, in particular T1-weighted (T1-w) and Diffusion weighted (DW)-MRI [4].

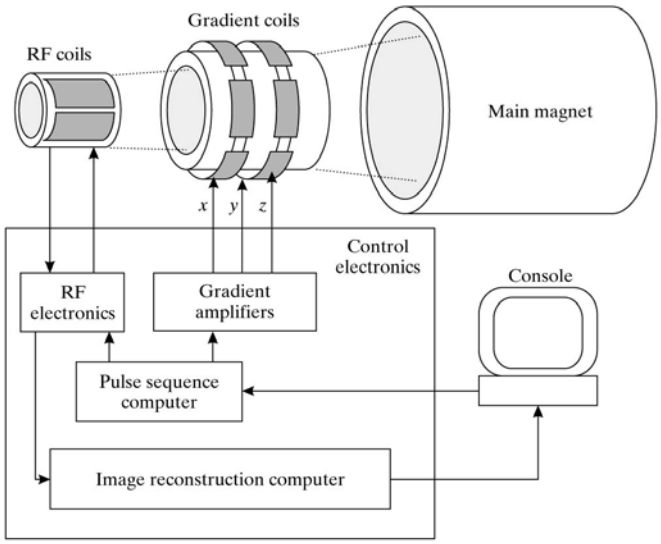

Figure 1.8: Principal components of a MRI scanner

Diffusion weighted-MRI

DW-MRI is currently the only technique capable of mapping the fibre architecture of tissue (e.g. nervous tissue, muscle) *in vivo*, since it carries information about tissue microstructure. In DW-MRI the mechanism of interest is the spin phase change resulting from components of incoherent displacement of spins along the axis of the applied field gradient.
We define as *diffusion time* Δ the time the protons are allowed to diffuse, and as *apparent diffusivity* the mean squared displacement (1.16) per unit time of the molecules

$$\langle (x(t) - x_0)^2 \rangle \tag{1.16}$$

where $x(t)$ is the position of the molecule at a given moment in time. The longer is Δ and the higher is the apparent diffusivity, the more the molecules will distribute over different distances from the origin with different associated phase shifts. This phase dispersion leads to a loss of signal coherence and therefore to a reduction in signal amplitude. By comparing the signal amplitude with and without the diffusion-encoding gradient applied, we can isolate the portion of dephasing resulting from incoherent motion.
The signal attenuation depends on:

1. the distribution of displacements during Δ along the axis of the applied gradient;

2. the gradient strength and its duration δ, which determine the sensitivity of the signal phase towards displacement.

Since Δ, δ and gradient strength are known and combined to derive the so-called *b-value*, we have a correlate for the motion of the diffusing particles along a particular axis.
The attenuation of the diffusion-weighted signal is sensitive to:

1. the general mobility of water molecules, depending on temperature, viscosity, presence of large molecules and many other factors;

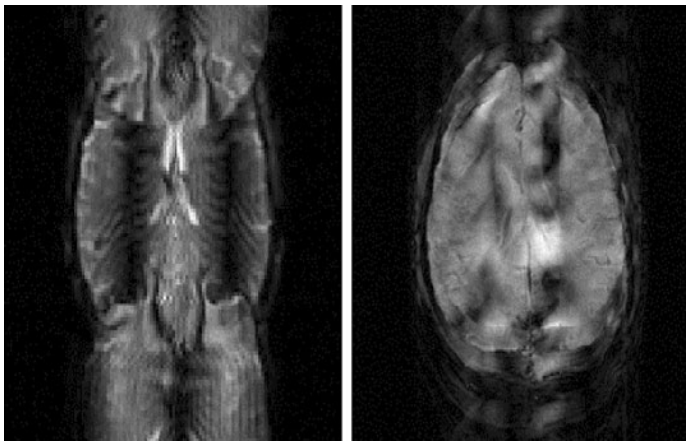

Figure 1.9: Typical motion artifact: ghosting and large signal variation across the image

2. barriers and obstacles imposed by microstructure, that slow down diffusion particles (hindered diffusion) or impose an upper limit on their overall mean-squared displacement (restricted diffusion).

Therefore DW MRI measurements reflect the amount of hindrance/restriction experienced by water molecules moving with a component of displacement along the axis of the applied gradient, averaged over the voxels.

1.1.3 Common MRI artifacts

An image artifact is any feature which appears in an image without being present in the original imaged object. Artifacts are typically classified as to their source, and there are many different kinds of them. Here we describe the two most common artifacts we always have to correct the images for [4, 5].

Motion artifacts

Motion artifacts are caused by involuntary movements (e. g. respiration, cardiac motion and blood flow, eye movements and swallowing) and minor movements of the subject during the imaging sequence. The results of motion are image blurring and ghost images appearance in the phase-encoding direction, as shown in Figure 1.9.

Eddy-current induced artifacts

When the diffusion gradient pulses are switched on and off, the time-varying magnetic field of the gradients result in current induction (eddy-currents) in the various conducting surfaces of the rest of the MRI scanner. These, in turn, set up magnetic field gradients that may persist after the primary gradients are switched off. Residual eddy-currents along the phase-encoding direction lead to a stretch/compression of the image along the phase-encode axis in DW-Echo Planar Imaging (EPI) images, as shown in Figure 1.10. The Magnetic Resonance (MR) signal intensity is proportional to the volume of the voxel, and thus an eddy-current of this type will artefactually reduce/increase the signal intensity.

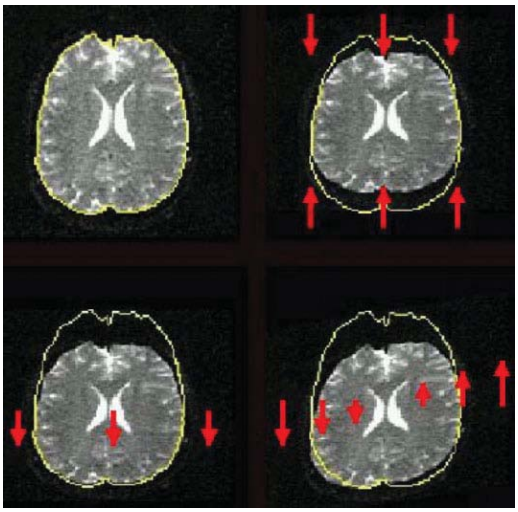

Figure 1.10: Three modes of distortion resulting from eddy-currents: contraction (top right), shift (bottom left), shear (bottom right)

1.2 The brain

In this section we describe the anatomy of the brain [6], and the study of connectome [7, 8].

1.2.1 Anatomy of the brain

The brain is a bilaterally symmetric, soft, gelatinous structure surrounded by its meninges and enclosed in the cranium. It is continuous with the spinal cord through the foramen magnum at the base of the skull.
The brain is subdivided into five continuous regions, from rostral to caudal: the *telencephalon*, *diencephalon*, *mesencephalon*, *metencephalon* and *myelencephalon*. As the brain grows in size and complexity, these regions fold upon and over one another, so that in the adult the evidence of these subdivisions is no longer clearly apparent. If the adult brain is viewed in three dimensions, only three regions are clearly visible, and these are the *cerebrum*, *cerebellum* and part of the *brain stem*.

Cerebrum

The cerebrum, observed from above, is composed of two large, oval, *cerebral hemispheres* (Figure 1.11). The hemispheres are narrower posteriorly, at the *occipital pole*, than anteriorly, at the *frontal pole*, and they are incompletely separated by the *longitudinal cerebral fissure*. The floor at the cerebral fissure is formed by the *corpus callosum*, a large myelinated fibre tract that forms an anatomical and functional connection between the right and left hemispheres.
The surface few millimeters of the cerebral hemisphere are composed of a highly folded collection of GM, known as the *cerebral cortex*. This folding increases the surface area and presents elevations, *gyri*, and depressions, *sulci*. Deep to the cortex is a central core of WM that forms the bulk of the cerebrum and represents fibre tracts, supported by neuroglia, ferrying information destined for the cortex and cortical responses to other regions of the Central Nervous System (CNS). Buried

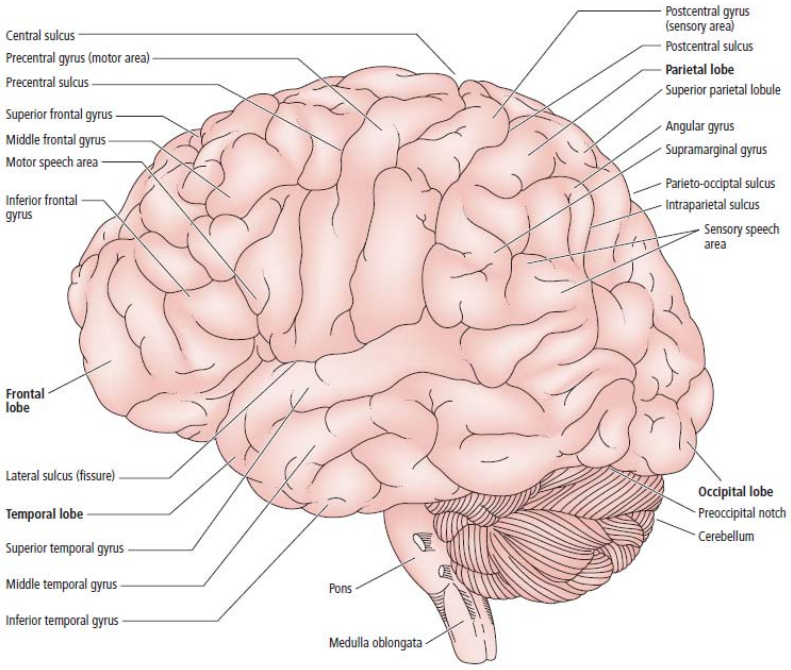

Figure 1.11: Diagram of the brain from a lateral view

within the mass of WM there are collections of neuron cell bodies, some of which are referred to as *basal ganglia*. Large collections of WM are also present in the diencephalons, i.e. the epithalamus, thalamus, hypothalamus and subthalamus.
The cerebrum is a hollow structure and the cavities within the cerebral hemispheres are called the *right* and *left lateral ventricles*, which communicate with the third ventricle via the *intraventricular foramen*.

Lobes of the cerebral hemispheres Each cerebral hemisphere is subdivided into five lobes: *frontal*, *parietal*, *temporal* and *occipital lobes*, and the *insula*. Additionally, the cortical constituents of the limbic system are also considered to be a region of the cerebral hemisphere forming a sixth *limbic lobe*. Lobes anatomy is described in Table 1.1.
Each lobe has a specific function: frontal lobes are associated with reasoning, motor skills, high level cognition, expressive language and motor function; parietal lobes are associated with processing of the body's senses; temporal lobes are responsible for sounds and language interpretation, and formation of memories; occipital lobes are associated with interpreting visual stimuli and information; insulae are involved in consciousness, functions related to emotions and regulation of the body's homeostasis; limbic lobes play a role in formation of spatial memory and new memories, regulation of heart rate and blood pressure, cognitive and attentional processing.

Histology of the cerebral cortex The cerebral cortex is well endowed with neurons, neuroglia, nerve fibres and a rich vascular supply. The histological organization of the cerebral cortex permits its subdivision into three regions: the *archicortex*, *mesocortex* and *neocortex*.
The archicortex is composed of only three layers and is located in the limbic system. The mesocortex is composed of three to six layers and is located predominantly in

Lobe	Surface	Major gyri
Frontal	Lateral	Precentral gyrus, inferior frontal gyrus
	Medial	Anterior paracentral lobule
	Inferior	Gyrus rectus, orbital gyri
Parietal	Lateral	Postcentral gyrus, superior parietal lobule, inferior parietal lobule
	Medial	Posterior paracentral lobule precuneus
Temporal	Lateral	Superior temporal gyrus, middle and inferior temporal gyri
	Superior	Transverse temporal gyri
	Inferior	Fusiform gyrus
Occipital	Lateral	Superior and inferior occipital gyri
	Medial	Cuneate gyrus (cuneus), lingual gyrus
Insula	Lateral	Short and long gyri
Limbic	Medial	Cingulate gyrus, parahippocampal gyrus, hippocampal formation, subcallosal, parolfactory and preterminal gyri

Table 1.1: Lobes of the cerebral hemispheres

the insula and cingulate gyrus. The neocortex is composed of six layers and comprises the bulk of the cerebral cortex.
Although the cortex is arranged in layers, it is functionally organized in *cell columns*. Each cell column is less than 0.1 mm in diameter, is perpendicular to the superficial surface of the cortex, passes to each of the six cortical layers, and is composed of neurons with similar functions. All neurons of a single column respond to like stimuli from the same region of the body.

White Matter of the cerebral hemispheres There are three categories of myelinated nerve fibres in the cerebral hemispheres: *commissural*, *projection* and *association fibres*. Commissural fibres are bundles of axons that connect the right and left cerebral hemispheres. The largest group of commissural fibres is the corpus callosum. Projection fibres are restricted to a single hemisphere and connect the cerebral hemispheres with lower levels, i.e. the corpus striatum, diencephalum, brain stem and spinal cord. The association fibres connect regions of a hemisphere to other regions of the same hemisphere.

Cerebellum

The cerebellum is located below the occipital lobe of the cerebral hemispheres. It is connected to the brain stem via the superior, middle and inferior cerebellar penducles. The cerebellum is responsible for coordination and balance.

Brain stem

The brain stem is between the spinal cord and the rest of the brain. Basic functions like sleep and breathing are controlled here.

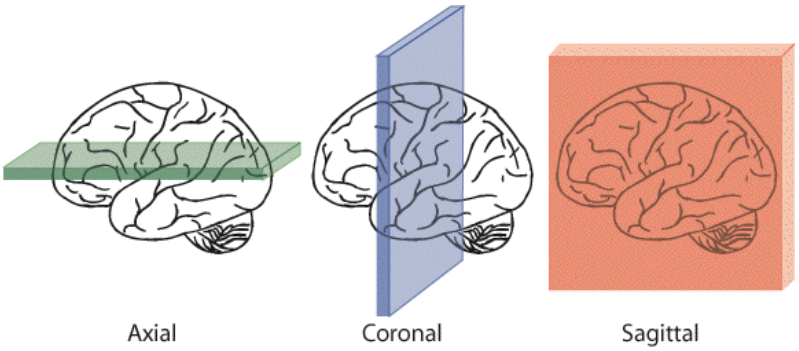

Figure 1.12: The three planes of section in the brain

1.2.2 MRI images of the brain

Clinical images use anatomic coordinate system for collection and presentation of the images. In this system there are three axes referenced to the body: left-right (L/R), superior-inferior (S/I) and anterior-posterior (A/P). Images planes used in neuroimaging are defined with reference to anatomic coordinate system (Figure 1.12):

- *axial* plane: perpendicular to the long axis of the body, defined by L/R and A/P axes;
- *coronal* plane: bisecting the front of the body from the back, defined by L/R and S/I axes;
- *sagittal* plane: bisecting the left and right sides of the body, defined by S/I and A/P axes.

1.2.3 Brain connectivity

Brain connectivity refers to a pattern of anatomical links, of statistical dependencies or of causal interactions between distinct units within a nervous system. Depending on the level of scale considered, the units correspond to individual neurons, neuronal populations, or anatomically segregated brain regions. The connectivity pattern is formed by structural links such as synapses or fibre pathways, or it represents statistical or causal relationships measured as cross-correlations, coherence, or information flow.
Neural activity is constrained by connectivity, understanding the connectivity pattern thus is crucial to elucidate how neurons and neural networks process information.

Modes of brain connectivity

Three modes can be distinguished: anatomical, functional and effective connectivity. Although in this work we will not refer to effective connectivity, we briefly introduce all the modes.
Anatomical connectivity refers to a network of structural connections linking sets of neural units. This pattern is relatively stable on a short time scale (seconds to minutes), i.e. the structural connectivity of a subject is likely to be reproducible if

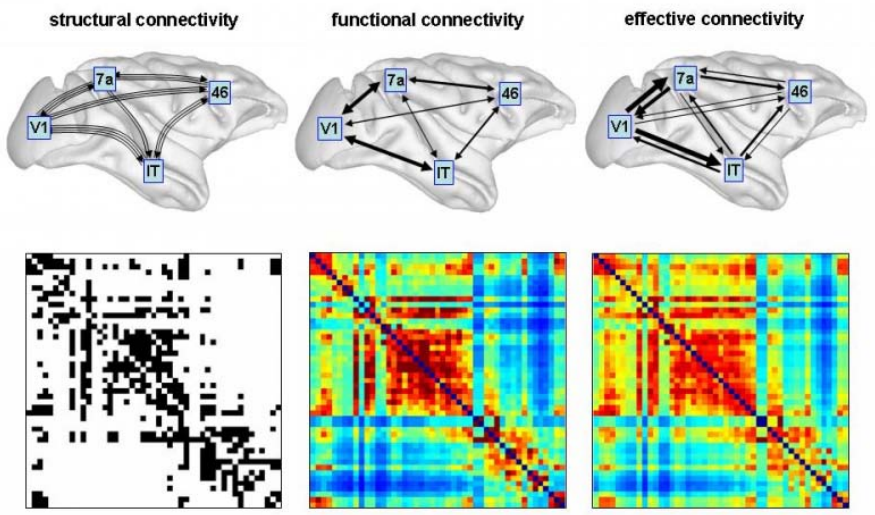

Figure 1.13: Modes of brain connectivity and connection matrices

measured within short periods of time, but likely to be subject to significant morphological change and plasticity at longer time scales (hours to days).
Functional connectivity is fundamentally a statistical concept. It estimates statistical dependence between neural units by measuring correlation or covariance, spectral coherence or phase-locking. Functional connectivity is often calculated between all the elements of a system, regardless of whether these elements are connected by direct structural links. Functional connectivity is highly time-dependent, because it is also influenced by the activity that the brain is engaged into.
Effective connectivity describes the influence of one neural unit over another.

Representation of connectivity patterns

Brain connectivity patterns can be represented in graph or matrix format (Figure 1.13). Structural brain connectivity forms a sparse and directed graph. The graph may be weighted, with weights representing connection densities or efficacies, or binary, with binary elements indicating the presence or absence of a connection. Functional brain connectivity forms a full symmetric matrix, with each of the elements encoding statistical dependence or proximity between two neural units. Such matrices may be thresholded to yield binary undirected graphs. Effective brain connectivity yields a full non-symmetric matrix. Applying a threshold to such matrices yields binary directed graphs.

Analysis of brain connectivity

Brain connectivity may be studied and analyzed using a broad range of network analysis approaches, in particular graph theory. Graphs are composed of vertices, corresponding to neural units, and edges, corresponding to pathways or statistical dependencies between the elements. Graphs are mathematically represented by adjacencies, and can be quantitatively examined for graph theory measures.
One important concept while studying brain connectivity is the one of *segregation*

and *integration*. Segregation in a network corresponds to the propensity of that network to form cliques of highly connected nodes, which are relatively weakly connected to the rest of the network. On the other hand an integrated network is a network where it is on average relatively easy to reach any node from any other node. From a biological point of view, highly integrated networks are strongly synchronized, since the activity of one node will largely influence most of the nodes in a network. Computationally speaking, segregation can be quantified by Clustering Coefficient (CC), transitivity, Local Efficiency (El) and modularity. Integration is measured in terms of characteristic path length or Global Efficiency (Eg).
Networks that preserve a certain level of segregation, while holding a high level of integration are referred to as *small world networks*. The human brain, at least at a macro-scale, is a small world.

1.3 Multiple Sclerosis

In this section we briefly describe the Multiple Sclerosis (MS) disease, and why we can consider brain anatomical connectivity study as a tool for the characterization of MS [8, 9].

Definition

MS is considered to be an immune-mediated disease in which the body immune system attacks the CNS, that is made up of the brain, spinal cord and optic nerves. The exact antigen remains unknown, which is why MS is considered by many experts to be immune-mediated rather than autoimmune.
Whithin the CNS, the immune system attacks myelin, the fatty substance that surrounds and insulates the nerve fibres, as well as the nerve fibres themselves. The damaged myelin forms scar tissue called *sclerosis*, which give the disease its name. When any part of the myelin sheath or nerve fibre is damaged or destroyed, nerve impulses traveling to and from the brain and spinal cord are distorted or interrupted, producing a wide variety of symptoms. The disease is thought to be triggered in a genetically susceptible individual by a combination of one or more environmental factors.
People with MS typically experience one of four disease courses, which can be mild, moderate or severe:

- Relapsing-Remitting (RR) MS is the most common disease course, characterized by clearly defined attacks of worsening neurological function. These attacks, also called relapses, flare-ups or exacerbations, are followed by partial or complete recovery periods (remissions), during which symptoms improve partially or completely and there is no apparent progression of disease. Approximately 85% of people with MS are initially diagnosed with relapsing-remitting RR MS;

- Secondary-Progressive (SP) MS follows after the RR MS. Most people who are initially diagnosed with RR MS will eventually transition to SP MS, which means that the disease will begin to progress more steadily (although not necessarily more quickly), with or without relapses;

- Primary-Progressive (PP) MS is characterized by steadily worsening neurological function from the beginning. Although the rate of progression may vary over time with occasional plateaus and temporary, minor improvements, there are no distinct relapses or remissions. About 10% of people with MS are diagnosed with PP MS.

- Progressive-Relapsing (PR) MS, the least common of the four disease courses, is characterized by steadily progressing disease from the beginning and occasional exacerbations along the way. People with this form of MS may or may not experience some recovery following these attacks; the disease continues to progress without remissions.

Epidemiology

MS most often appears in young adulthood, with the incidence peaking around age 30. It occurs more commonly in women than in men, at a ratio approximately 3:1. The disease is common in areas inhabited by people of northern European ancestry. It is more common in Europe, the United States, Canada, New Zealand, and some parts of Australia; it is much less common in Asia and rare in tropical and subtropical regions. The global distribution of MS increases with distance north or south of the equator, although there is some evidence that the north-south incidence gradient may have disappeared in the northern hemisphere.
Around 2,5 million of people in the world have MS. In Europe 520,000 suffer from the disease, 100,000 in the UK and 58,500 in Italy[2].

MS and brain connectivity

MS lesions appear both in WM and GM, and studies using either GM correlation or tractography reported important alterations of network organization. Therefore, comparison of same anatomical brain networks in healthy subjects and patients can be a tool for enabling earlier and more precise diagnosis of disease and understanding its pathophysiology in vivo. Those are key aspects to guarantee a better treatment.

[2]Multiple Sclerosis Society `http://www.mssociety.org.uk/`, Lega Italiana Sclerosi Multipla O.N.L.U.S. `http://www.lism.it`

Chapter 2

Work and methods

In this chapter we present the general methodology used to determine quantitative measures from a data set of structural T1-w and DW MRI images. The results obtained with our specific data set are reported and discussed in Chapter 3.
In this work the measures of interest were: thickness of the cerebral cortex, Fractional Anisotropy (FA) of fibres connecting pairs of distinct cortical regions. These values were respectively used to represent GM (Section 2.1) and WM (Section 2.2) connectivity of a relevant brain structural sub-network.
With the results we wanted to test the following hypotheses:

1. in healthy subjects GM has the same connectivity pattern of the underlying WM;

2. observation of the same patterns in healthy subjects and SP MS patients leads to a measurable effect of network efficiency loss caused by the disease.

2.1 Cortical GM connectivity

Structural MRI provides information about anatomical brain connectivity. Many methods have been proposed for dividing and classifying the whole connectivity network derived from anatomical measures into connected influential sub-networks, since most cognitive functions involve only a subset of brain regions. One of these techniques [1], based on the Principal Component Analysis (PCA), is applied to the whole connectivity matrix to obtain a set of coherent sub-networks, called Principal Networks (PNs), starting from values of thickness of cortical areas. As reported in previous studies [10], between-subject correlation of cortical thickness of two brain regions can be regarded as a measure of their connectivity. In fact, if two areas show similar anatomical features over subjects, this might stem from the interaction between underlying neuronal substrates through their anatomical connections. In addition, the evolution in the structure of cerebral cortex is thought to reflect the subdivisions underpinning brain functioning [11].
In this section we explain how we measured the thickness of the cortical Regions of Interest (Subsection 2.1.1), how we used these values to calculate the Principal Networks (Subsection 2.1.2), and how we cross-validated our results (Subsection 2.1.3).

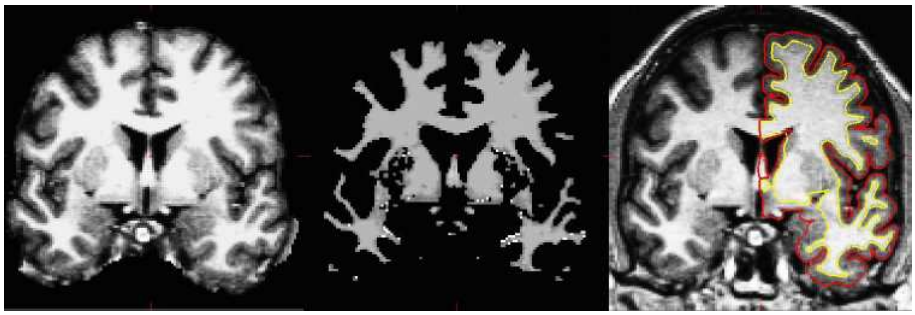

Figure 2.1: Three stages of FreeSurfer surface-based stream. Skull-stripped image (left); WM segmentation (centre); white surface, yellow line, and pial surface, red line, overlaid on the original volume (right)

2.1.1 FreeSurfer cortical reconstruction

We pre-processed the T1-w images with FreeSurfer [12, 13], a software application developed at the Martinos Center for Biomedical Imaging. FreeSurfer is a set of software tools for the study of cortical and subcortical anatomy. Its reconstruction process is divided in surface-based and volume-based stream [14]. The process has an accuracy of 0.2 mm compared with postmortem measures of cortical thickness and has been validated using different scanners and MRI protocols.

Surface-based stream

The surface-based pipeline consists of several stages [15, 16]. First, the volume is registered with the *Talairach atlas*, a coordinate system of the human brain that describes the location of structures independently from individual differences in the size and overall shape of the brain. This affine registration allows FreeSurfer to use Talairach coordinates as seed points in the later stages.
The $\overrightarrow{B}_1$ bias field, a low-frequency and very smooth signal that corrupts MRI images, is estimated by measuring the variation in the WM intensity. The main body of the WM is used to estimate the field across the entire volume. Likely WM points are chosen based on their locations in Talairach space as well as on their intensity and the local neighborhood intensities. The intensity at each voxel is then divided by the estimated bias field at that location in order to remove the effect of the bias field.
The skull is stripped (Figure 2.1, left) using a deformable template model [17]. Voxels are then classified as WM or something other than WM (Figure 2.1, centre) based on intensity and neighbor constraints. Cutting planes are chosen to separate the hemispheres from each other as well as to remove cerebellum and brain stem. The cutting planes location is based on the expected Talairach location of corpus callosum and pons, as well as several rules-based algorithms that encode the expected shape of these structures.
Then *white surface* is generated for each hemisphere by tiling the outside of the WM mass for that hemisphere, and refined to follow the intensity gradients between WM and GM. The white surface is then nudged to follow the intensity gradients between the GM and CSF and create the *pial surface* (Figure 2.1, right). The distance between the white and the pial gives us the thickness at each location of cortex [13].

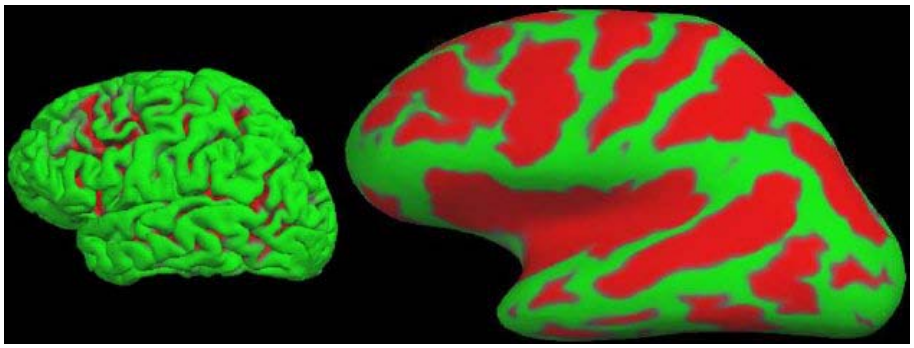

Figure 2.2: Left: pial surface. Right: Inflated surface. Green indicates a gyrus, red indicates a sulcus.

We can also compute the local curvature, surface area, and the surface normal. A 3D view of the pial surface is shown in Figure 2.2 (left). This surface can be inflated to show the areas in the sulci as shown in Figure 2.2 (right). This surface can then be registered to the spherical atlas based on the folding patterns [18].

Volume-based stream

The volume-based subcortical stream is designed to preprocess MRI volumes and label subcortical tissue classes. The stream consists of five stages [12].
The first stage is an affine registration with Talairach space specifically designed to be insensitive to pathology and to maximize the accuracy of the final segmentation: a different procedure than the one employed by the surface-based stream. This is followed by an initial volumetric labeling.
The variation in intensity due to the $\overrightarrow{B}_1$ bias field is corrected, again using a different algorithm than the surface-based stream.
Finally, a high dimensional nonlinear volumetric alignment to the Talairach atlas is performed. After the preprocessing, the volume is labeled. The volume-based stream only depends upon the skull stripping to create a mask of the brain in which the labeling is performed. The last stage, actually labeling the volume, is described below.
Both the cortical [12] and the subcortical [19] labeling use the same basic algorithm. The final segmentation is based on both a subject-independent probabilistic atlas and subject-specific measured values. The atlas is built from a training set, i.e., a set of subjects whose brains (surfaces or volumes) have been labeled by hand. These labels are then mapped into a common space (Talairach space for volumes and spherical space for surfaces) to achieve point-to-point correspondence for all subjects. A "point" is a voxel in the volume or a vertex on the surface. At each point in space, there is the label that was assigned to each subject and the measured value (or values) for each subject. Three types of probabilities are then computed at each point. First, the probability that the point belongs to each of the label classes is computed. The second type of probability is computed from the spatial configuration of labels that exist in the training set, which is termed the neighbourhood function. The neighbourhood function is the probability that a given point belongs to a label given the classification of its neighbouring points. The neighbourhood function is important because it helps to prevent islands of one structure in another at the structure edges. Third, the Probability Distribution Function (PDF) of the

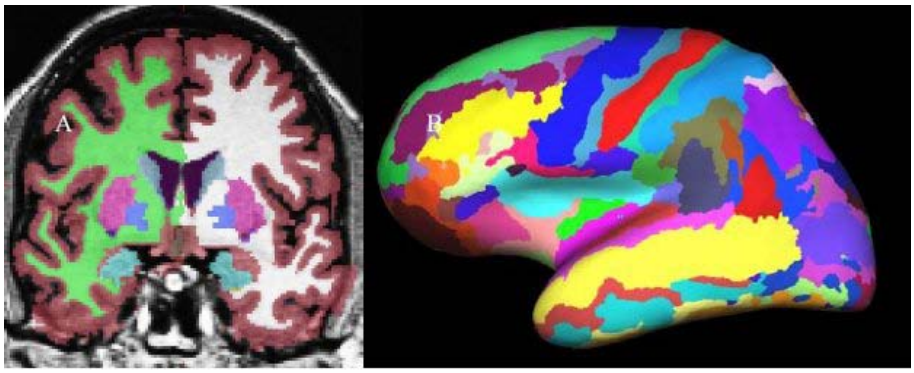

Figure 2.3: Left: volume-based labelling. Right: surface-based labelling.

measured value is estimated separately for each label at each point. For volume-based labeling, the measured value is the intensity at that voxel. For surfaced-based labeling, the measured value is the curvature in each of the principal directions at that vertex. The PDF is modeled as a normal distribution, so we only need to estimate the mean and variance for each label at each point in space. If there is more than one measured value (e.g., multi-spectral data), then the PDF is modeled as a multivariate normal for which we need to estimate the mean and variance-covariance matrix for each label.
The classification of each point in space to a given label for a given data set is achieved by finding the segmentation that maximizes the probability of input given the prior probabilities from the training set. First, the probability of a class at each point is computed as the probability that the given class appeared at that location in the training set times the likelihood of getting the subject-specific measured value from that class. The latter is computed from the PDF for that label as estimated from the training set. The probability of each class at each point is computed. An initial segmentation is generated by assigning each point to the class for which the probability is greatest. Given this segmentation, the neighbourhood function is used to recompute the class probabilities. The data set is resegmented based on this new set of class probabilities. This is repeated until the segmentation does not change. This procedure allows the atlas to be customized for each data set by using the information specific to that data set. Once complete, not only do we have a label for each point in space, but we also have the probability of seeing the measured value at each voxel. The product of this probability over all points in space yields the probability of the input. This will be used later during automatic failure detection. This procedure has been shown to be statistically indistinguishable from manual raters [19] and relatively insensitive to changes in acquisition parameters [20]. The results are shown in Figure 2.3.

Outputs of interest in our work

We evaluated the connectivity between 64 cortical regions segmented by FreeSurfer[1]. The segmentation is based on the *Desikan-Killany atlas* [21], which defines the regions as follows (Figure 2.4).

- Temporal lobe - medial aspect: enthorinal cortex, parahippocampal gyrus,

[1] According to [1] we did not consider the banks of the superior temporal gyrus.

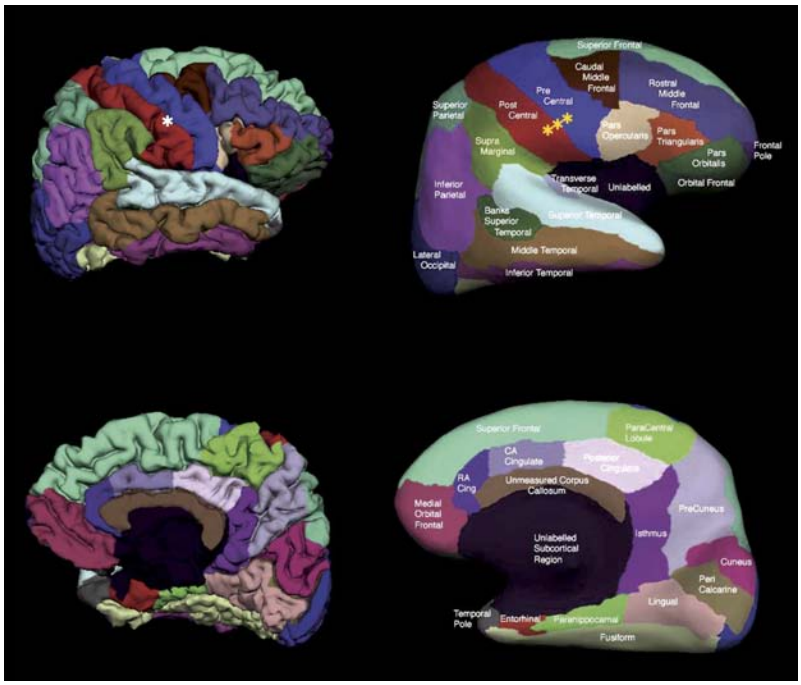

Figure 2.4: Pial (left) and inflated (right) cortical representations of the regions of interest in one hemisphere. The top row illustrates the lateral view of the hemisphere while the bottom row shows the medial view of the hemisphere. The white asterisk on the pial surface (left) indicates the cortex around the perimeter of the central sulcus that is buried within the gyri and thus not visible. The yellow asterisks on the inflated surface (right) indicate the cortex around the perimeter of the central sulcus that has been "inflated" and is now visible.

temporal pole, fusiform gyrus.

- Temporal lobe - lateral aspect: superior temporal gyrus, middle temporal gyrus, inferior temporal gyrus, transverse temporal gyrus, banks of the superior temporal gyrus.
- Frontal lobe: superior frontal gyrus, middle frontal gyrus, inferior frontal gyrus, orbitofrontal gyrus, frontal pole, precentral gyrus, paracentral gyrus.
- Parietal lobe: postcentral gyrus, supramarginal gyrus, superior parietal cortex, inferior parietal gyrus, precuneus.
- Occipital lobe: lingual gyrus, pericalcarine cortex, cuneus, lateral occipital cortex.
- Cingulate cortex: rostral anterior division, caudal anterior division, posterior division, isthmus division.

The correspondence between regions names and indexes is given in Table 2.1. From now on, we will always refer to this notation.

Manual checking and editing

FreeSurfer often requires manual intervention to correct for mistakes that affect the cortical thickness calculation. Two main kinds of error can occur in the WM

Region name	**Index**	
	Left hemisphere	Right hemisphere
caudal anterior cingulate cortex	1	33
caudal middle frontal gyrus	2	34
cuneus	3	35
entorhinal cortex	4	36
fusiform gyrus	5	37
inferior parietal gyrus	6	38
inferior temporal gyrus	7	39
cingulate gyrus, isthmus	8	40
lateral occipital cortex	9	41
lateral orbitofrontal cortex	10	42
lingual gyrus	11	43
medial orbitofrontal gyrus	12	44
middle temporal gyrus	13	45
parahippocampal gyrus	14	46
paracentral gyrus	15	47
inferior frontal gyrus, pars opercularis	16	48
inferior frontal gyrus, pars orbitalis	17	49
inferior frontal gyrus, pars triangularis	18	50
pericalcarine cortex	19	51
postcentral gyrus	20	52
posterior cingulate gyrus	21	53
precentral gyrus	22	54
precuneus	23	55
rostral anterior cingulate cortex	24	56
rostral middle frontal gyrus	25	57
superior frontal gyrus	26	58
superior parietal gyrus	27	59
superior temporal gyrus	28	60
supramarginal gyrus	29	61
frontal pole	30	62
temporal pole	31	63
transverse temporal gyrus	32	64

Table 2.1: Correspondence between region names and indexes

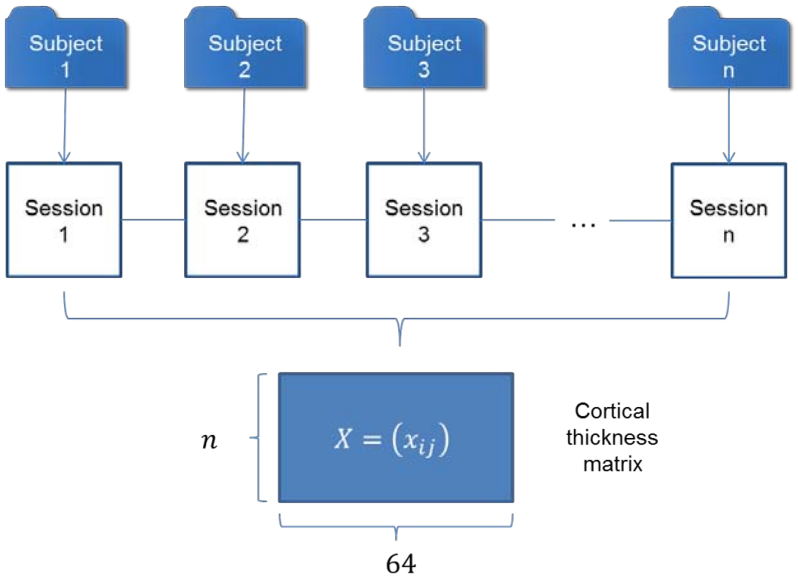

Figure 2.5: Creation of the cortical thickness data matrix

segmentation process:

- voxels that should be WM are excluded, or voxels that should not be WM are included in error;
- the intensity normalization step fails because the proper intensity for WM cannot be determined.

The first issue can be fixed with a manual deletion or addition of voxels in the WM volume [22]. The second can be fixed by adding a *control point* to indicate a location that should be included in the WM boundary, and therefore normalized at the same intensity value [23].
After editing, the cortical reconstruction process must be repeated, starting from the steps that involve the WM segmentation file.

2.1.2 Principal Networks calculation

In this section we describe the process for calculating the PNs [1]. All the functions involved in the process are part of the TractoR project [24]. TractoR works with R [25], a free software for statistical computing and graphics, and provides packages for reading, writing and visualizing MR images files of different formats including the Neuroimaging Informatics Technology Initiative (NIfTI) one.

Preliminary operations

Firstly, with the `tractor.session` package, we organized in a list of sessions the analysis directories created by FreeSurfer. Then, with the `tractor.graph` package, we created the cortical thickness data matrix $X = (x_{ij})$. Each row of X corresponded to a subject, and each column corresponds to a cortical region: the element x_{ij} was the thickness of the j-th cortical region in the i-th subject (see Figure 2.5). X was then center and scaled in order to have zero mean ($\mu = 0$) and unit variance ($\sigma^2 = 1$) in each cortical region. The result was the normalized matrix $\hat{X} = (\hat{x}_{ij})$.

Whole brain connectivity matrix

We calculated $A = (a_{ij})$, the cross-subject correlation matrix corresponding to $\hat{X}$. We considered A directly as the 64×64 full association matrix that describes the whole connectivity network of the brain: the correlation value $-1 \leq a_{ij} \leq 1$ is an indirect measure of connectivity between cortical regions i and j.
Given two variables X and Y describing the thickness of two cortical areas observed in the n subjects, their degree of correlation was calculated via the Pearson's correlation coefficient (ρ). The value of ρ is defined as the covariance of the two variables divided by the product of their standard deviations:

$$\rho = \frac{cov(X,Y)}{\sigma_X \sigma_Y} = \frac{E[(X - \mu_X)(Y - \mu_Y)]}{\sigma_X \sigma_Y}$$

The resulting value is in the range $[-1, 1]$, where 1 indicates total positive correlation, 0 indicates no correlation and -1 indicates total negative correlation.

Principal Component Analysis

In order to obtain the relevant sub-networks in the brain, we processed A with a PCA-based decomposition. The block diagram is represented in Figure 2.6. Being A real and symmetric by construction, we could diagonalize it:

$$A = QLQ^{-1} \tag{2.1}$$

L was a diagonal matrix of eigenvalues l_k $(1 \leq k \leq 64)$ of A, Q was a matrix with the eigenvectors of A as columns.
To obtain the k-th partial association matrix $A^k = (a^k_{ij})$, where $1 \leq k \leq 64$, we calculated the product in (2.1) setting to zero every eigenvalue of L but the k-th. Being Q orthogonal by construction, also the following equation was valid

$$a^k_{ij} = l_k Q_{ik} Q_{jk} \quad 1 \leq i, j \leq 64$$

With the technique presented above, the component matrices were calculated through a linear decomposition of the full association matrix, therefore:

$$A = \sum_{k=1}^{64} A^k$$

2.1.3 Leave-one-out cross-validation

In order to cross-validate the results within the data set, we used a leave-one-out based method. We applied it to evaluate the reliability of the main PN described by $A^1 = (a^1_{ij})$.
We formed n groups, the t-th group comprising all of the subjects of the original data set but the t-th $(1 \leq t \leq n)$. Then we calculated $A^1|_t = (a^1_{ij})|_t$ for each one of the n groups.
We determined a probability matrix $P = (p_{ij})$ and a difference matrix $D = (d_{ij})$.

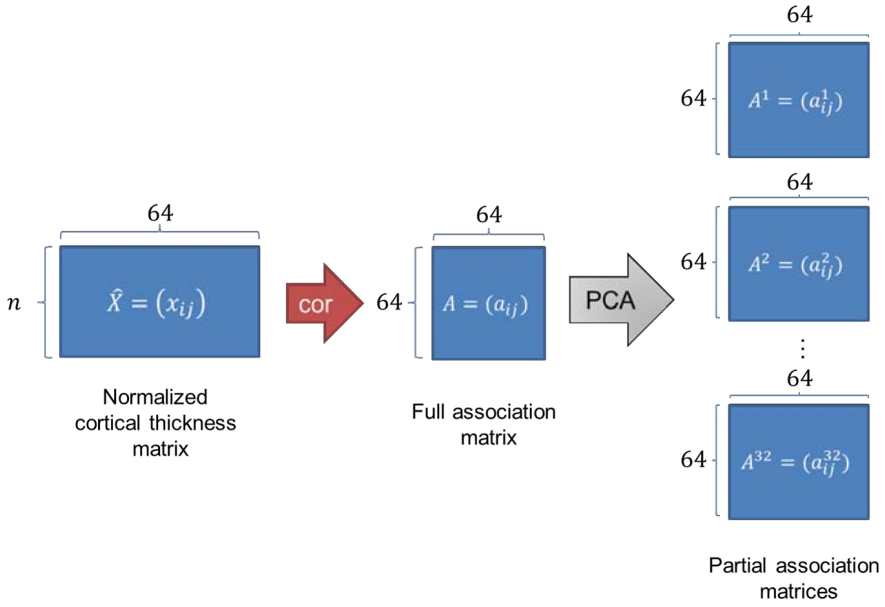

Figure 2.6: Calculation of the partial association matrices

P contained the frequencies of appearance of the connections in the leave-one-out iterations:

$$p_{ij} = \frac{\sum_{t=1}^{n} y_{ij}|_t}{n} \quad 1 \leq i, j \leq 64$$

where

$$y_{ij}|_t = \begin{cases} 0 & \text{if } a_{ij}^1|_t = 0 \\ 1 & \text{if } a_{ij}^1|_t \neq 0 \end{cases} \quad 1 \leq i, j \leq 64$$

D evaluated the difference in calculating the connections from the full data set or by using the leave-one-out approach. Its elements were determined by the absolute difference between the elements of A^1 and the corresponding mean elements resulting from the leave-one-iterations:

$$d_{ij} = \left| a_{ij}^1 - \frac{\sum_{t=1}^{n} a_{ij}^1|_t}{n} \right|$$

P and D were visually inspected, and their information combined in the reliability assessment of the results.

2.2 Sub-cortical WM connectivity

Given the cortical regions of Table 2.1, we evaluated the connectivity of the underlying WM by processing the DW MRI data set.
After the pre-processing (Subsection 2.2.1), we analyzed the images with both Diffusion Tensor Imaging (DTI) MRI (Subsection 2.2.2) and probabilistic tractography (Subsection 2.2.3, Subsection 2.2.4). After performing the analyses on the single subjects, we combined the results of DTI and tractography to calculate a group measure of sub-cortical WM connectivity (Subsection 2.2.5).

Software We used the FMRIB Software Library (FSL), MATLAB®, MRtrix and NiftyReg:

- FSL is a comprehensive library of analysis tools for functional MRI, MRI and DTI brain imaging data [26, 27, 28].

- MATLAB® is a high-level language and interactive environment for numerical computation, visualization and programming [29].

- MRtrix is a set of tools for performing DW MRI White Matter tractography in presence of crossing fibres, using Constrained Spherical Deconvolution (CSD) and probabilistic streamlines algorithm [30, 31].

- NiftyReg is a NIfTI-library based program developed at the University College of London (UCL) [32]. It contains algorithms to perform rigid, affine and non-linear registration of images. The rigid and affine registration are performed using an algorithm called Aladin [33, 34], which is based on a block-matching approach and a Trimmed Least Squares scheme. The non-rigid image registration implementation is based on the Free-From Deformation [35].
  In this work, we always applied the transformations to the images along with a nearest-neighbour interpolation.

2.2.1 DW-MRI data pre-processing

First we corrected the DW scans for eddy-currents induced distortions and for simple head motion. We used the FSL Eddy Current Correction tool setting the zero volume as a reference for the affine registration algorithm. Since the affine registration can produce a rotation of the image, we equally rotated the encoding vectors with the script reported in Listing 4.1 in the Code listing appendix.
We split the DW four-dimensional data in several three-dimensional files, then we used FSL Brain Extraction Tool (BET) [36] to determine the brain mask and delete non-brain tissue from images of the first volume. We set the fractional intensity threshold to 0.3 and the vertical gradient to the default zero value.
Because NIfTI files cannot carry in the header the *gradient scheme*, which describes direction and b-value for each volume, with MATLAB® we put the information in a separate text file.
We registered all the de-skulled diffusion images to a common space using the FMRIB's Linear Image Registration Tool (FLIRT) [37, 38]. Then with BET we deleted non-brain tissue from the T1-w image, using the same parameters used for the DW data set. Finally, with FLIRT we registered the de-skulled anatomical image to the same common space. Registrations were based on a transformation with six degrees of freedom, nearest neighbour interpolation and performed with the script Listing 4.2 reported in the Code listing appendix.

2.2.2 Tensor-derived parametric maps

We applied a DTI-based analysis [39] to the pre-processed DW data set to generate whole brain parametric maps.

Diffusion Tensor MRI

Diffusion Tensor (DT) MRI is a technique used to estimate the effective diffusion tensor D from a series of DW images, and to analyze and display the information it contains in each voxel. The estimate is obtained by using a relationship between the measured echo attenuation in each voxel and the applied magnetic field sequence. The attenuating effect of all gradient waveforms applied in all three directions, x, y and z, is summarized in a symmetric b-matrix, which is calculated for each DW image. The formula relating the effective diffusion tensor to the measured echo is:

$$\ln \frac{A(b)}{A(b=0)} = -\sum_{i=1}^{3}\sum_{j=1}^{3} b_{ij}D_{ij} = -Trace(bD) \tag{2.2}$$

where $A(b)$ and $A(b = 0)$ are the echo magnitudes of the diffusion weighted and non-diffusion weighted signals respectively, and b_{ij} is a component of the b-matrix. Each DW image and the corresponding b-matrix are used to estimate D from (2.2).

Quantitative parameters

DT MRI provides quantitative parameters that can be derived with a geometric approach. In particular, we are interested in the Fractional Anisotropy, which is obtained from the second moment of the distribution of the eigenvalues of D. The FA characterizes the anisotropy of the diffusion process. The value, comprised between 0 and 1, is calculated as:

$$FA = \sqrt{\frac{3}{2}}\frac{\sqrt{(\lambda_1 - \hat{\lambda})^2(\lambda_2 - \hat{\lambda})^2(\lambda_3 - \hat{\lambda})^2}}{\sqrt{\lambda_1^2 + \lambda_2^2 + \lambda_3^2}}$$

where λ_i is the i-th eigenvalue of D, and $\hat{\lambda} = (\lambda_1 + \lambda_2 + \lambda_3)/3$.

Fractional Anisotropy parametric map

First we converted the brain mask image in the diffusion space to the bitwise data type. Then with MRtrix we generated the DT images from the DW images, supplying our own encoding file, and we calculated the diffusion tensor FA parametric map. As we will explain later, the creation of a FA map is also required by the fibre tracking algorithm implemented in MRtrix.

2.2.3 Creation of Regions of Interest masks

In order to investigate the relationship between the connectivity in GM and underlying WM, we focused on a subset of cortical regions. We chose the most connected areas included in the first Principal Network, i.e. the regions whose connectivity value was described at least at the 50% by the inclusion in the first PN. We considered these regions both in the left and the right hemisphere.
For each area of Table 2.2, we created a binary mask of the corresponding subcortical WM in the DW space as the intersection of the dilated WM mask with the dilated cortical Region Of Interest (ROI) mask. We performed dilation and

Region name	Index	
	Left hemisphere	Right hemisphere
fusiform gyrus	5	37
inferior parietal gyrus	6	38
lateral orbitofrontal cortex	10	42
precuneus	23	55
rostral anterior cingulate cortex	24	56
rostral middle frontal gyrus	25	57
superior frontal gyrus	26	58

Table 2.2: Subset of regions considered for the analysis of WM connectivity

Region name	Label(s)
white matter	2, 41
cerebellum	7, 8, 46, 47
brain stem	16
corpus callosum	251, 252, 253, 254, 255
fusiform gyrus	1007, 2007
inferior parietal gyrus	1008, 2008
lateral orbitofrontal cortex	1012, 2012
precuneus	1025, 2025
rostral anterior cingulate cortex	1026, 2026
rostral middle frontal gyrus	1027, 2027
superior frontal gyrus	1028, 2028

Table 2.3: Correspondence between region names and labels

intersection of masks by using FSLmaths, a FSL tool that allows mathematical manipulation of images.
We also created the masks of regions to be excluded while investigating WM tracts. We used FSLmaths to create two unique exclusion masks to be used while tracing contralateral or ipsilateral tracts, the first given by the sum of cerebellum and brain stem, the second given by the sum of cerebellum, brain stem and corpus callosum.

Labels extraction

We created the binary masks of selected cortical areas, WM, cerebellum, brain stem and corpus callosum by extracting the corresponding labels from the FreeSurfer segmentation files. Since there is only one label at each voxel, we were guaranteed not to have overlap between different regions. The correspondence between ROIs and labels is described in Table 2.3[2]
FreeSurfer generates segmentations in the Gaussian Classifier Atlas (GCA), a $1mm^3$, 256^3 normalized anatomical space: we calculated the transformation from the GCA to the DW space and applied it to the segmentations before extracting the labels. We calculated the transformations with the pipeline derived from [40] and described below.

[2]The complete list of the labels is available at `https://surfer.nmr.mgh.harvard.edu/fswiki/FsTutorial/AnatomicalROI/FreeSurferColorLUT`

1. Non-linear transformation from $1mm^3$ GCA to $1mm^3$ T1-w image. We used FreeSurfer and the procedure described in [41].

2. Affine transformation from $1mm^3$ T1-w to $1 \times 1 \times 3$ mm pseudo-T1-w image. The pseudo-T1-w image was generated by subtracting the proton density image from the T2-weighted (T2-w) scan, using a rigid body registration. As a result, the pseudo-T1-w image and the T2-w image were inherently coregistered.

3. Non-linear transformation from $1 \times 1 \times 3$ mm T2-w image to $1mm^3$ image in the diffusion space (b=0).

4. Non-linear transformation from $1mm^3$ image in the diffusion space (b=0) to $2mm^3$ image in the diffusion space (b=0).

All the transformations were calculated using de-skulled images in NIfTI format, matching the orientation of the standard templates [42]. Transformations from 2 to 4 were calculated with NiftyReg and saved to be used also in later stages of our work.

2.2.4 Probabilistic tractography analysis

In nervous tissue the term *fibre* refers to one or several WM axons. Fibre pathways can be reconstructed from DW data using the *tractography* technique [4]: continuous longer-range trajectories of fibres are reconstructed from local, discrete estimates of their orientation. The discrete estimates are described by an Orientation Density Function (ODF) estimated from the DW data. None of the tractography methods is capable of reconstructing nerve fibres or even fibre bundles: they compute trajectories or pathways through the data, to which a large portion of the nerve fibres run reasonably in parallel.
The fundamental assumption underpinning tractography is that the tangent to the space curve traced by fibre tract is always and everywhere parallel with the local peak of the ODF. Moreover, as the local ODF is discretely sampled on the voxel grid, the reconstruction of continuous trajectories from these discrete estimates requires interpolation of the data. Additional assumptions can be made regarding, for example, the fibre stiffness and the local curvature, and upper limits can be specified for these values while reconstructing the continuous trajectories.
Estimates of fibre orientation can be obtained either through the diffusion Orientation Density Function (dODF) or the fibre Orientation Density Function (fODF). In this work we used the second method.

Direct estimation of the fODF

The method presented in [43] – implemented in MRtrix – is able to estimate directly the distribution of fibre orientations within a voxel from high angular resolution DW-MRI data without making prior assumptions regarding the number of fibre populations present.
During a typical DW experiment, the average displacement of water molecules is expected to be of the order of 10μm, and the radius of curvature of curved fibres greater than 10μm. For this reason the method assumes that

1. during the time of the experiment there is *no exchange* between spatially distinct fibre bundles, or between orientationally distinct sections of the same fibre bundle;

2. all fibre populations found in the brain have *identical diffusion characteristics*.

As a consequence of assumption 1, the measured DW signal is well approximated by the sum of signals emanating from regions that differ for spatial location or orientation. Moreover, assumption 2 implies that the diffusion profiles of any two distinct and coherently oriented WM populations are identical in all apart from their orientation. Thus, the DW signal attenuation measured from a single coherently oriented fibre population can be represented by an axially symmetric response function $R(\theta)$, defined such as the fibres are aligned with the z axis, where θ is the elevation angle in spherical coordinates. $R(\theta)$ can be determined directly from the data by measuring the DW profile in regions likely to contain a single coherently oriented fibre population, i. e. those with the highest diffusion anisotropy.
The DW signal attenuation measured from a sample containing several distinct fibre populations can be written as

$$S(\theta, \phi) = \sum_i f_i \hat{A}_i R(\theta) \tag{2.3}$$

that is the sum of the response function of each population, weighted by their respective volume fractions f_i, and rotated such as they are aligned with their respective orientations. $\hat{A}_i$ is the operator representing the rotation onto the direction (θ, ϕ_i), where ϕ is the azimuthal angle in spherical coordinates.
The signal of equation (2.3) can be expressed as the convolution over the unit sphere of the response function $R(\theta)$ with a fibre Orientation Density Function $F(\theta, \phi)$:

$$S(\theta, \phi) = R(\theta) \otimes F(\theta, \phi) \tag{2.4}$$

The fODF of equation (2.4) gives the fraction of fibres within the sample that are aligned along the direction (θ, ϕ), and therefore contains all the information given by the parameters f_i in (2.3).
During a high-angular resolution DW experiment, $S(\theta, \phi)$ is sampled along a large number of directions. If $R(\theta)$ is known a priori, then the fODF can be obtained by performing the spherical deconvolution of $R(\theta)$ from $S(\theta, \phi)$.

Spherical deconvolution

The spherical deconvolution operation can be formulated as the action of an ensemble of rotations on a function defined over a sphere. The n-th order spherical harmonic representation of $S(\theta, \phi)$ is given by:

$$\underline{S}^n = \mathbf{R}^n \underline{\mathbf{F}}^n \tag{2.5}$$

$\underline{\mathbf{F}}^n$ is a vector of length $(2n+1)$ representing the n-th order Spherical Harmonic (SH) decomposition of $F(\theta, \phi)$. The SHs form a complete orthonormal basis set of functions over the sphere. Each SH can be denoted by two numbers: its harmonic order n ($n \geq 0$), and phase factor m ($-n \leq m \leq n$).
$\mathbf{R}^n$ is a $(2n + 1) \times (2n + 1)$ matrix representing the n-th order Rotational Harmonic (RH) decomposition of $R(\theta)$. RHs form a orthonormal basis over the space of

pure rotations. Each RH is denoted by three numbers: a harmonic order n ($n \geq 0$), and two phase factors m and l ($-n \leq m, l \leq n$). The SH representation of $S(\theta, \phi)$ can be obtained using a simple linear least squares fit.
The spherical deconvolution operation can be performed by simply inverting each $\mathbf{R}^n$ matrix in (2.5) to recover $\underline{\mathbf{F}}^n$.
The maximum harmonic order n_{max} that can be reliably estimated is limited by the number of available independent samples of the signal attenuation profile. For example, with $n_{max} = 8$, the number of parameters to be estimated is 45, so the diffusion encoding scheme must contain at least 45 non collinear directions. Moreover, the spherical deconvolution operation is more sensitive to noise for higher harmonic orders, so the higher harmonic components need to be attenuated (low-pass filtered) or discarded.
MRtrix implements the CSD [44], a method to perform spherical deconvolution that preserves the angular resolution while remaining robust to noise effects. This is done by placing a non-negativity constrain of the estimated fibre orientation density, as negative fibre orientation densities are physically impossible. This constrain eliminates the need for low-pass filtering of the higher harmonic components.

Generation of fibre tracts between two ROIs

The tracts between pairs of ROIs were traced with MRtrix, after the application of the required preliminary operations [45], which are listed below.
We created a mask of high FA voxels. These were assumed to contain single-fibre voxels, and used in the response function estimation. The mask was created with an initial erosion step to ensure that no edge voxels with artefactually high FA were included in the single-fibre mask. This mask was then applied to the FA map, and the resulting image was thresholded at FA=0.7. The resulting mask contained a few hundred voxels, all located within high FA WM regions.
Then, we estimated the SH coefficients of the response function, $R(\theta)$, from the DW signal in the single fibre voxels, $S(\theta, \phi)$.
Finally, for each voxel we calculated the fODF, $F(\theta, \phi)$, by using the CSD and setting to 8 the maximum harmonic order, n_{max}. We also used a brain mask to prevent unnecessary computations in non-brain voxels and speed up the computation time.
We generated the tracts by specifying a seed and a target ROI mask of sub-cortical WM. We always included the brain mask and the appropriate exclusion mask to prevent the algorithm to trace the tracts in regions not anatomically compatible. We set to 2000 the number of repetitions: the algorithm stopped either after having traced 2000 tracts or after attempting 200000 times to trace a path between the ROIs.

2.2.5 Tract-specific Diffusion Tensor derived metrics

We used the individual outputs of tractography to create a group binary map of each tract in a reference atlas, the de-skulled version of the Linear International Consortium for Brain Mapping (ICBM) Average Brain (ICBM152) Stereotaxic Registration Model. This is a version of the ICBM Average Brain, an average of 152 T1-w MRI scans, linearly transformed to Talairach space, with $1mm^3$ resolution [46, 47, 48].
MRtrix saves the tracts in a custom tck file format and bitwise data type: we converted the files to the NIfTI format and 32-bit floating point data type. As a

reference template we used the $2mm^3$ image in the diffusion space (b=0).
In order to register the tract to the Linear ICBM Average Brain, with NiftyReg we calculated the transformations listed below.

1. Non-linear transformation from the $2mm^3$ image in the diffusion space (b=0) to the $1mm^3$ image in the diffusion space (b=0).
2. Non-linear transformation from the $1mm^3$ diffusion space to the $1 \times 1 \times 3$ mm T2-w image.
3. Affine transformation from the $1 \times 1 \times 3$ mm pseudo-T1-w to the T1-w image.
4. Non-linear transformation from the $1mm^3$ T1-w image to the Linear ICBM Average Brain.

After the registration, we created a robust binary map of each tract in the common space. First, we thresholded the tract to remove voxels with connectivity probability value lower than 0.2. We chose the threshold value according to the literature [49, 50] and we considered only the image values comprised between the 2% and 98% percentiles.
Then, we binarized the tract, and calculated a group mask by summing the masks created for all the subjects. This first group mask was thresholded again to remove the voxels with a connectivity probability value lower than 0.7. We chose this threshold because with more conservative values we were not able to delete non anatomically feasible tracts from the final mask.

Calculation of single tracts metrics

We applied the masks to the parametric maps created in Subsection 2.2.2 to characterize each tract with its FA value. First, we registered the masks created above to the $2mm^3$ resolution diffusion space of each subject with the following pipeline.

1. Non-linear transformation from the Linear ICBM Average Brain to the T1-w image.
2. Non-linear transformation from $1mm^3$ GCA to $1mm^3$ T1-w image.
3. Affine transformation from $1mm^3$ T1-w to $1 \times 1 \times 3$ mm pseudo-T1-w image.
4. Non-linear transformation from $1 \times 1 \times 3$ mm T2-w image to $1mm^3$ image in the diffusion space (b=0).
5. Non-linear transformation from $1mm^3$ image in the diffusion space (b=0) to $2mm^3$ image in the diffusion space (b=0).

For the steps from 2 to 5 we used the same transformations calculated in Subsection 2.2.3.
After we registered the tracts, we applied the subject WM mask to delete badly registered voxels from the final result. The WM mask of each subject was created as described below.

1. Segmentation of T1-w image with FSL FMRIB's Automated Segmentation Tool (FAST) Graphical User Interface (GUI). We used the program default parameters and required one image per class as an output.

2. Multiplication of the WM binary mask by 100.

Then, we registered the masks to the $2mm^3$ image in the diffusion space (b=0), applied a 70 threshold value and binarized it again.
For each subject, we determined the FA value associated to each tract by masking the corresponding FA map. Finally, we calculated the mean FA value of each tract across all the subjects to obtain a group measure of sub-cortical WM connectivity.

Chapter 3

Results and discussion

In this chapter we present the results of our analysis, which was performed on a data set of healthy controls and patients affected by SP MS. In Section 3.1 we talk about the acquisition protocols, then in Section 3.2 we describe in detail the steps of our work, the results we obtained and the conclusions we derived from them.

3.1 Data set

Our data set comprised 32 healthy controls and 13 patients affected by Secondary-Progressive MS. The cohort of patients had been recruited as part of a study to investigate GM involvement in MS at the NMR Research Unit, UCL Institute of Neurology, UCL, London, UK. This work was reviewed and approved by the National Research Ethics Service (NRES) Committee London-Queen Square. All patients gave written informed consent. Each of them underwent a High Angular Resolution Diffusion Imaging (HARDI) [51], a dual echo proton density/T2-w and a T1-w MRI scan of the brain. Images were acquired with a Philips Achieva 3T system (Philips Healthcare, Best, The Netherlands), using a 32-channel head coil.
HARDI scan consisted of a cardiac-gated Spin Echo (SE) EPI imaging sequence acquired axial-oblique and aligned with the anterior commissure (AC)-posterior commissure (PC) line. Scans were acquired with 2mm isotropic voxel size, 61 isotropically distributed diffusion-weighted directions with b = 1200s/mm^2, 7 non diffusion-weighted [b = 0] volumes, T_E = 68ms, T_R = 2400ms [depending on the cardiac rate], Sensitivity Encoding (SENSE) factor = 3.1.
Dual echo proton density/T2-w axial-oblique scans were acquired aligned with the AC-PC line, with 1mm × 1mm × 3mm voxel size, T_R = 3500ms, T_E = 19/85ms.
Three-dimensional sagittal T1-w Fast Field Echo (FFE) [52] scan was acquired with 1mm isotropic voxel size, T_R = 6.9ms, T_E = 3.1ms.

3.2 Descriptive and quantitative analysis

First we built our data set of cortical parameters: values were taken from a previous work carried out at UCL [53] in which they had been collected from FreeSurfer. In that work, a scoring system was implemented to select subjects in which FreeSurfer had a good performance. We visually checked FreeSurfer WM segmentations of healthy controls, manually editing them when required as described in Subsection 2.1.1. As a result, more than half of the subjects required minor refinements of the WM segmentation, especially in the temporal lobes area. In Table 3.1 we give a statistical description of the final cortical thickness data set, with expected value and standard deviation of cortical thickness for each area. These values were consistent with published literature.

3.2.1 Analysis of connectivity in the GM

We reorganized the values of cortical thickness in two matrices: a 32×64 matrix for values of healthy controls and a 13×64 matrix for values of SP MS patients. Then, we calculated the two full association matrices describing whole brain connectivity respectively in controls and patients.

Calculation of the first PN

We analyzed the connectivity between areas of GM by processing the data of healthy subjects with the method of Subsection 2.1.2. We hypothesized patterns of connectivity found to be relevant in the controls, the PNs, would have a different characterization in the patients. While calculating the PNs, we applied a loading threshold of 0.1 to the vertices and an absolute correlation threshold of 0.2 to the edges of the corresponding graphs. The R script and function implementing the PNs analysis are in the Code listing appendix, respectively in Listing 4.3 and Listing 4.4. Based on the functions implemented by the TractoR project, the code was written by the author of the thesis to be used with our specific data set.
The full association matrices of controls and patients are shown in Figure 3.1. We ordered the rows and columns of the matrices according to the influence of the cortical regions over the first PN. The influence of the i-th region was quantified by the *loading* value Q_{i1}, i.e. the i-th element of the eigenvector corresponding to the main eigenvalue (see equation (2.1)). We observed that the influence of gyral regions over the first PN reflected the real structure of the original controls' association matrix. In fact, as a result of the sorting, the highest values of correlation were grouped close to the bottom left corner, while the lowest values were grouped close to the top right corner of the matrix. Significantly, we did not observe the same structure of connectivity in the full association matrix of the patients. That was an evidence for the presence of disease-related modifications in the connectivity of the GM. Moreover, we observed that the range of correlation values assumed by the connections was larger in the patients than in healthy subjects. In the group of controls the range was $\simeq [-0.23, 1]$, while it was $\simeq [-0.65, 1]$ in the group of SP MS patients.
Though, when we compare the results of a same analysis performed on controls and patients, we should remember that the two groups had different size. In fact, the number of patients was about a third of the number of controls, so the outcome could be biased due to this fact. This must be kept in mind also while observing

Region name	**Cortical thickness statistics healthy controls**		**Cortical thickness statistics SP MS patients**	
	Left	Right	Left	Right
caudal anterior cingulate cortex	2.61 ± 0.33	2.65 ± 0.26	2.53 ± 0.29	2.68 ± 0.26
caudal middle frontal gyrus	2.26 ± 0.15	2.32 ± 0.14	2.15 ± 0.12	2.22 ± 0.08
cuneus	1.92 ± 0.16	1.88 ± 0.14	1.81 ± 0.10	1.74 ± 0.12
entorhinal cortex	3.47 ± 0.37	3.51 ± 0.35	3.41 ± 0.41	3.55 ± 0.43
fusiform gyrus	2.89 ± 0.19	2.76 ± 0.19	2.74 ± 0.10	2.68 ± 0.09
inferior parietal gyrus	2.42 ± 0.13	2.33 ± 0.16	2.32 ± 0.13	2.28 ± 0.09
inferior temporal gyrus	2.80 ± 0.20	2.68 ± 0.23	2.74 ± 0.13	2.67 ± 0.07
cingulate gyrus, isthmus	2.64 ± 0.26	2.63 ± 0.19	2.46 ± 0.20	2.42 ± 0.19
lateral occipital cortex	2.22 ± 0.13	2.22 ± 0.16	2.08 ± 0.13	2.14 ± 0.12
lateral orbitofrontal cortex	2.51 ± 0.16	2.69 ± 0.18	2.39 ± 0.16	2.57 ± 0.15
lingual gyrus	2.13 ± 0.13	2.16 ± 0.14	1.93 ± 0.10	1.92 ± 0.08
medial orbitofrontal gyrus	2.31 ± 0.20	2.54 ± 0.17	2.23 ± 0.14	2.51 ± 0.15
middle temporal gyrus	2.70 ± 0.19	2.87 ± 0.22	2.64 ± 0.11	2.75 ± 0.10
parahippocampal gyrus	3.05 ± 0.35	2.92 ± 0.28	3.06 ± 0.47	2.88 ± 0.31
paracentral gyrus	2.37 ± 0.12	2.28 ± 0.16	2.26 ± 0.08	2.15 ± 0.13
inferior frontal gyrus, p. opercularis	2.41 ± 0.16	2.49 ± 0.18	2.28 ± 0.12	2.33 ± 0.13
inferior frontal gyrus, p. orbitalis	2.47 ± 0.22	2.58 ± 0.22	2.40 ± 0.23	2.58 ± 0.20
inferior frontal gyrus, p. triangularis	2.24 ± 0.17	2.38 ± 0.17	2.10 ± 0.15	2.24 ± 0.14
pericalcarine cortex	1.63 ± 0.13	1.64 ± 0.12	1.43 ± 0.10	1.40 ± 0.10
postcentral gyrus	1.96 ± 0.13	1.91 ± 0.14	1.86 ± 0.14	1.82 ± 0.13
posterior cingulate gyrus	2.62 ± 0.16	2.56 ± 0.16	2.54 ± 0.19	2.46 ± 0.12
precentral gyrus	2.40 ± 0.13	2.39 ± 0.16	2.24 ± 0.07	2.28 ± 0.12
precuneus	2.46 ± 0.14	2.40 ± 0.18	2.33 ± 0.16	2.24 ± 0.16
rostral anterior cingulate cortex	2.71 ± 0.30	3.03 ± 0.22	2.66 ± 0.14	2.94 ± 0.33
rostral middle frontal gyrus	1.98 ± 0.12	2.17 ± 0.13	2.00 ± 0.08	2.13 ± 0.10
superior frontal gyrus	2.47 ± 0.15	2.60 ± 0.14	2.37 ± 0.09	2.44 ± 0.08
superior parietal gyrus	2.13 ± 0.12	2.05 ± 0.12	2.04 ± 0.14	2.03 ± 0.14
superior temporal gyrus	2.71 ± 0.19	2.84 ± 0.19	2.57 ± 0.16	2.63 ± 0.12
supramarginal gyrus	2.44 ± 0.13	2.36 ± 0.16	2.33 ± 0.11	2.29 ± 0.12
frontal pole	2.51 ± 0.26	2.49 ± 0.26	2.36 ± 0.15	2.47 ± 0.24
temporal pole	3.72 ± 0.30	3.58 ± 0.34	3.60 ± 0.34	3.54 ± 0.15
transverse temporal gyrus	2.39 ± 0.19	2.46 ± 0.23	2.15 ± 0.17	2.17 ± 0.22

Table 3.1: Mean and standard deviation [mm] of cortical thickness data

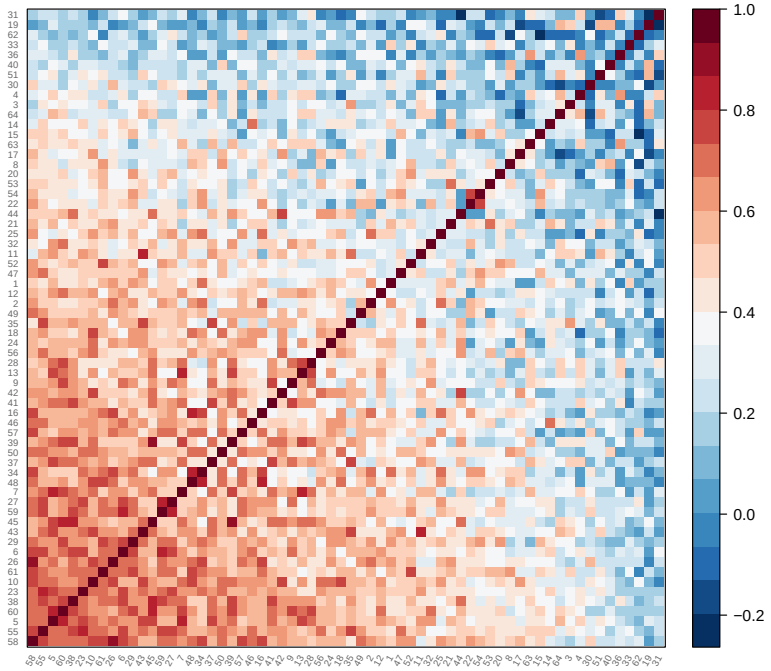

(a) Healthy controls

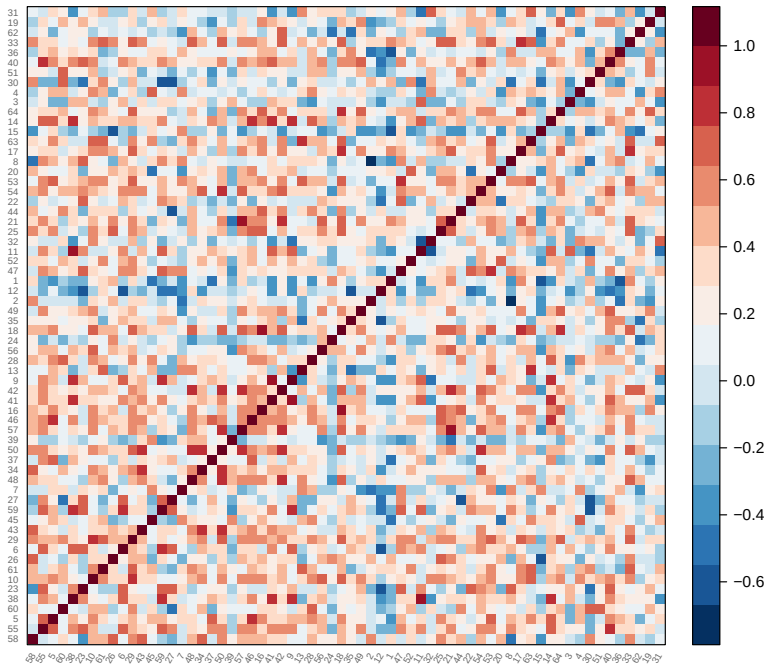

(b) SP MS patients

Figure 3.1: Full association matrices: cortical regions are ordered according to their loadings over the first PN of healthy controls

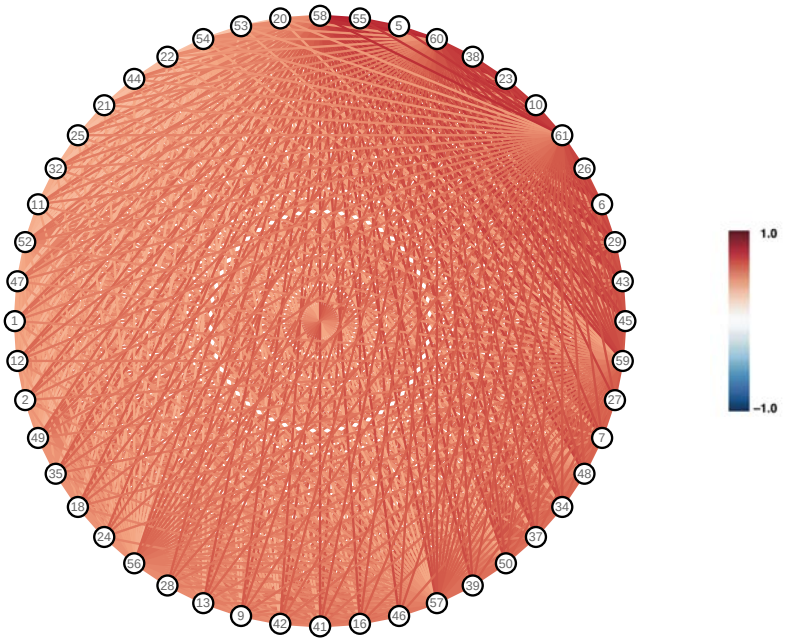

Figure 3.2: Graph representation of the controls first PN, based on cortical thickness data: only vertices and edges above loading and weight thresholds are shown. The vertices are organized in a circular structure for visual clarity, and ordered according to their loading

the results of the following steps.
In Figure 3.2 we show the graph representation of the controls' first PN, with regions ordered according to their loadings. This fully-connected network comprised forty-eight regions out of sixty-four, and showed a broad tendency for positive correlation in agreement with [1]. We also noticed that the most part of regions interconnected by highly-weighted (> 0.5) edges already appeared in the first PN reported by [1]. For all the reasons just explained, we concluded that the PNs technique was reproducible with our data set. Differences in the results could be due to differences in the acquisition protocol of T1-w scans or to FreeSurfer cortical reconstruction process. As already mentioned before, FreeSurfer has an accuracy of 0.5mm and we were dealing with data in the range of $[0.5, 4]$mm.

Leave-one-out cross-validation

We cross-validated the first PN obtained from the previous analysis using the leave-one-out based approach described in Subsection 2.1.3. The code used to perform this step is part of the R script reported in the Code listing appendix as Listing 4.3. The results are shown in Figure 3.3. By comparing P and D with the graph representation of Figure 3.2, we observed that connections with less variable weights were assigned, or not, to the first PN with low uncertainty. The only exception, a group of four cortical areas (indexes: 22, 54, 53, 20), had very low influence over the original first PN. Not only the PNs method was reproducible, but its main result was also reliably calculated with our data set.

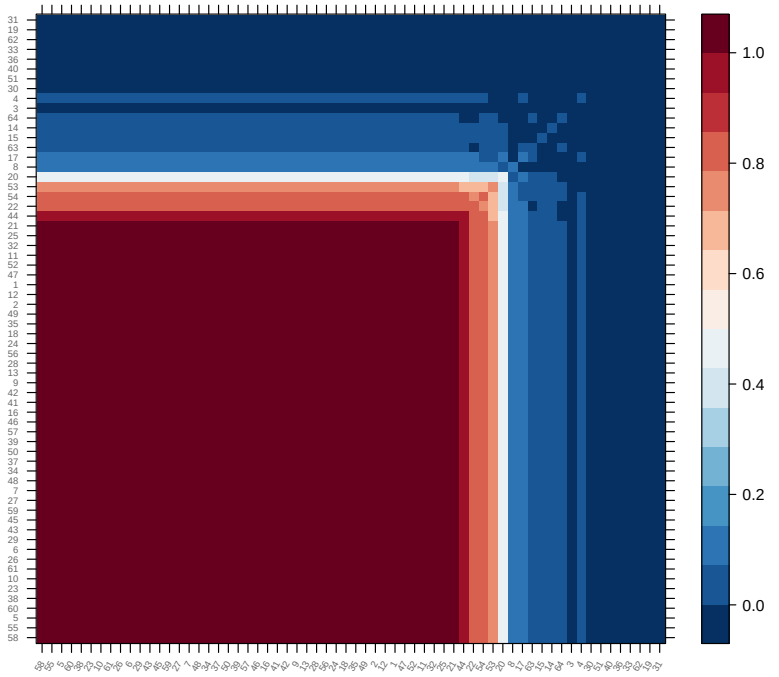

(a) Each element of the matrix $P = (p_{ij})$ shows the probability for the respective connection to appear in the first PN. The probability is based on the results of the leave-one-out

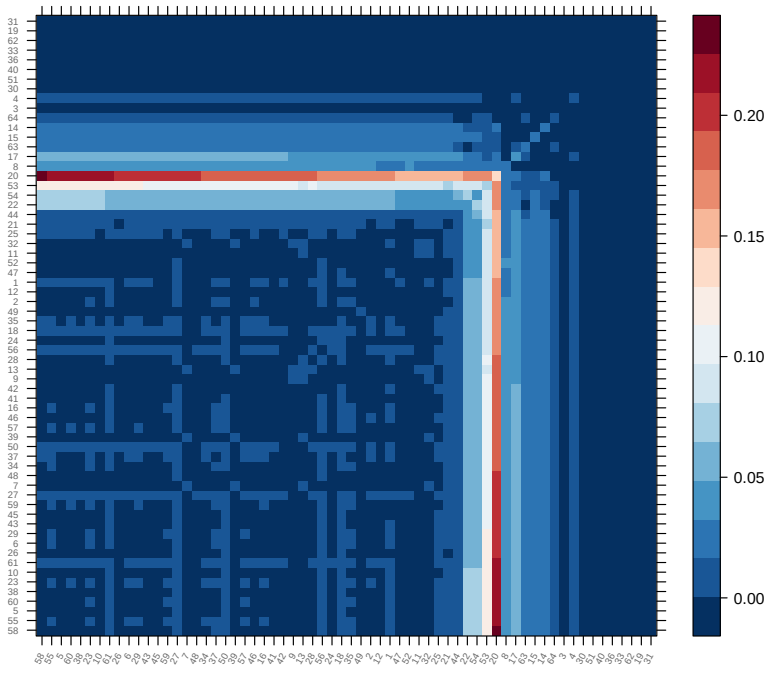

(b) Each element of the matrix $D = (d_{ij})$ shows the difference in calculating the respective connection of the first PN from the entire data set or as the mean value from the leave-one-out

Figure 3.3: First PN leave-one-out cross-validation. Cortical regions are ordered according to their loadings over the first PN of healthy controls

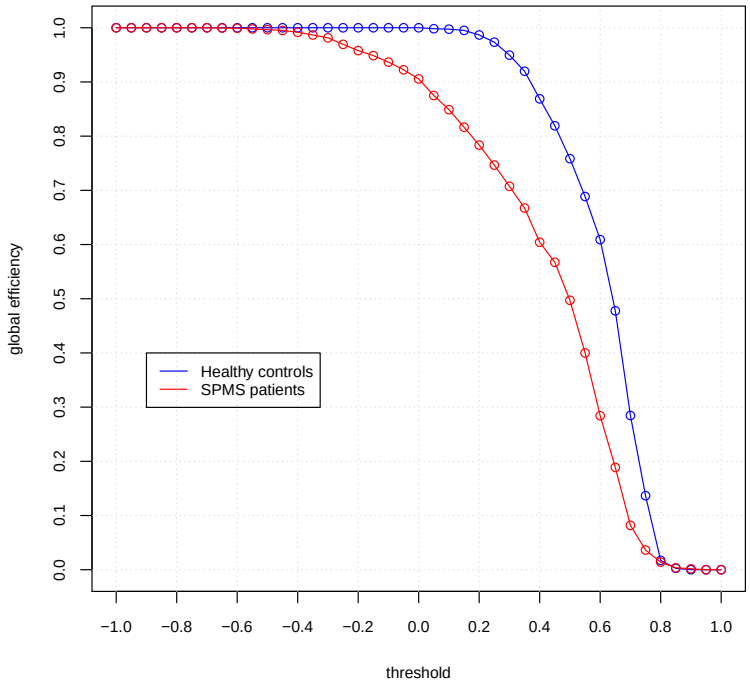

Figure 3.4: Global Efficiency of the first PN. The plot compares the Eg of the first PN for increasing values of threshold applied to the partial association matrices

Analysis of changes between the two groups

We considered the full association matrices of the two groups, and we extracted their portion describing connectivity between regions of the controls' first PN: to analyze changes of connectivity in the GM, we tested changes of Global Efficiency in the sub-graphs having controls' first PN areas as vertexes. Eg is given by

$$E_{global} = \frac{1}{N(N-1)} \sum_{i \neq j} \frac{1}{L_{i,j}}$$

where N is the number of nodes and $L_{i,j}$ is the length of the shortest path between i and j. From the formula written above, we see that Eg is a topological property, equal to 1 in a fully-connected network. In our case, the networks of both the groups were fully-connected, so we tested the changes of Eg by applying a set of increasing thresholds to the edges weights of the sub-graphs. Although thresholds were chosen with no physiological criterion, this method showed evidence of impaired global connectivity in the patients. In Figure 3.4 we show the two decreasing trends of Eg.

Given this result, we made a further investigation by applying the *Mann-Whitney U* test [54]. The aim was to understand which cortical regions had thickness values statistically different in the two groups. The Mann-Whitney U test is non-parametric, so it does not require any assumption about the distribution of the two samples. The test is applicable when all the observations from the two groups are independent from each other, and data are measured with an ordinal scale. With H_0 and H_1 respectively the null and the alternative hypothesis, and Me_i the median of the i-th

group, the test can be

- bilateral
$$H_0 : Me_1 = Me_2 \quad H_1 : Me_1 \neq Me_2$$
- unilateral
$$H_0 : Me_1 \geq Me_2 \quad H_1 : Me_1 < Me_2$$
or
$$H_0 : Me_1 \leq Me_2 \quad H_1 : Me_1 > Me_2$$

The test calculates the observed value u_{obs} of the statistic U, whose distribution under the null hypothesis is known, through the following steps:

1. data of the two distributions are increasingly ordered in a unique group, keeping trace of their original membership;
2. each datum is given a rank calculated as the times the datum is preceded by data of the other group (in presence of ties, the rank is the mean value of the possible ranks);
3. u and u' are respectively the sum of the numbers assigned to data of the first and second group;
4. u_{obs} is chosen as $min(u, u')$.

With n_1 and n_2 the size of the two samples, when n_1 or n_2 is greater than 15 U is approximately normally distributed. In that case, the standardized value

$$z = \frac{u_{obs} - \mu_U}{\sigma_U} \tag{3.1}$$

is a standard normal deviate whose significance can be checked in the tables of normal distribution. μ_U and σ_U are the expected value and the standard deviation in the null hypothesis H_0

$$\mu_U = \frac{n_1 n_2}{2} \quad \sigma_U = \sqrt{\frac{n_1 n_2 (n_1 + n_2 + 1)}{12}}$$

From the significance of (3.1) the test calculates the p_{value}. This is the probability of observing a value u_{obs} at least as extreme as the one actually observed, if the test statistic really were distributed as in H_0. Given a maximum false positive rate α, if $p_{value} \geq \alpha$ the null hypothesis is accepted. The test is available in the R software under the name of `wilcox.test`.
In our case we had one null hypothesis H_{0m} for each cortical region ($1 \leq m \leq 64$), and rejection of H_{0m} corresponded to declaring that region m was differentially characterized in the two groups. Since we wanted to control the global false positive rate, we applied the Bonferroni's correction and used a false positive rate $\alpha/64$ for each test. The results are shown in Table 3.2. For each region we calculated the relative percentage difference of cortical thickness as

$$\frac{\overline{thk}_{controls} - \overline{thk}_{patients}}{\overline{thk}_{controls}} \times 100$$

Region name	Cortical thickness statistics		Relative difference (%)
	Controls	SP MS patients	
lingual gyrus left	2.13 ± 0.13	1.93 ± 0.11	9.40%
paracentral gyrus left	2.38 ± 0.12	2.26 ± 0.08	4.96%
pericalcarine cortex left	1.63 ± 0.13	1.43 ± 0.10	12.32%
precentral gyrus left	2.40 ± 0.13	2.24 ± 0.10	7.02%
transverse temporal gyrus left	2.39 ± 0.19	2.15 ± 0.17	9.97%
lingual gyrus right	2.16 ± 0.14	1.92 ± 0.08	10.96%
pericalcarine cortex right	1.64 ± 0.12	1.40 ± 0.10	14.65%
superior frontal gyrus right	2.60 ± 0.14	2.44 ± 0.08	5.99%
superior temporal gyrus right	2.84 ± 0.19	2.63 ± 0.12	7.44%
transverse temporal gyrus right	2.46 ± 0.23	2.17 ± 0.22	11.94%

Table 3.2: Results of Mann-Whitney U test in the GM: we compared the cortical thickness mean values by calculating the percentage difference relative to healthy controls

where $\overline{thk}$ stands for the mean value of thickness. The three lowest values of relative percentage difference corresponded to the regions not individuated in both the hemispheres: paracentral, precentral and superior frontal gyri. We observed that, for our cohort of SP MS patients, loss of global GM efficiency was due to a process not strongly lateralized.

3.2.2 Analysis of connectivity in the WM

In the second part of our work we investigated the anatomical structure that underlies GM. We were interested in the pattern formed by WM fibres connecting specific pairs of cortical regions. For this study we considered all the 13 SP MS patients, and 31 out of the 32 healthy controls. One healthy control was discarded because files required to work in the diffusion space were not available.
As described in Section 2.2, we created a group mask of each tract and we applied it to the individual maps of FA. In this way we obtained a measure of connectivity for each fibre tract of interest. We investigated the relationship between connectivity in the GM and characteristics of the underlying WM through the study of the first PN. Since this network comprised a large number of cortical areas, we found a trade-off with the high computational times of tractography by restricting the analysis to the list of Table 2.2. We chose these areas for two reasons: assumed not to have significant lateralization of cortical thickness properties, they formed a highly inter-connected sub-network of the first PN; moreover, they are known to be part of the Default Mode Network (DMN), a relevant system of the brain. We thought it would be sufficient for our purposes to characterize connectivity properties of a meaningful subset of the first PN.
In Table 3.3 we have listed the expected value and standard deviation of the FA distributions measured in the two groups. We set to 0 the values corresponding to fibre tracts that were badly traced by the algorithm and therefore where the measures of FA would be inconsistent.
From the FA data we created two connection matrices to describe connectivity in the WM. The matrices are shown in Figure 3.5 with the cortical regions ordered

ROI index		**FA statistics**	
Seed	Target	Controls	SP MS patients
5	37	0.485 ± 0.023	0.400 ± 0.066
	6	0.419 ± 0.021	0.378 ± 0.024
	38	0.566 ± 0.023	0.489 ± 0.073
	10	0.458 ± 0.025	0.393 ± 0.041
	42	0	0
	21	0.416 ± 0.022	0.377 ± 0.031
	53	0.482 ± 0.030	0.417 ± 0.060
	23	0.412 ± 0.024	0.354 ± 0.040
	55	0.478 ± 0.023	0.405 ± 0.056
	24	0.471 ± 0.028	0.407 ± 0.041
	56	0	0
	26	0.466 ± 0.025	0.414 ± 0.029
	58	0.469 ± 0.026	0.408 ± 0.039
37	6	0.568 ± 0.018	0.489 ± 0.068
	38	0.418 ± 0.026	0.389 ± 0.028
	10	0	0
	42	0.465 ± 0.023	0.405 ± 0.044
	21	0.463 ± 0.026	0.411 ± 0.050
	53	0.414 ± 0.022	0.374 ± 0.036
	23	0.444 ± 0.022	0.382 ± 0.050
	55	0.426 ± 0.023	0.367 ± 0.047
	24	0	0
	56	0.486 ± 0.026	0.422 ± 0.043
	26	0.431 ± 0.024	0.381 ± 0.034
	58	0.471 ± 0.018	0.434 ± 0.032
6	38	0.599 ± 0.023	0.533 ± 0.060
	10	0.461 ± 0.023	0.418 ± 0.044
	42	0	0
	21	0.450 ± 0.022	0.416 ± 0.025
	53	0.490 ± 0.026	0.437 ± 0.055
	23	0.442 ± 0.022	0.400 ± 0.017
	55	0.569 ± 0.021	0.495 ± 0.046
	24	0.462 ± 0.023	0.418 ± 0.044
	56	0	0
	26	0.441 ± 0.019	0.431 ± 0.020
	58	0.443 ± 0.021	0.408 ± 0.034
38	10	0	0
	42	0.461 ± 0.021	0.420 ± 0.050
	21	0.490 ± 0.024	0.416 ± 0.025
	53	0.433 ± 0.020	0.437 ± 0.055
	23	0.568 ± 0.023	0.400 ± 0.017
	55	0.435 ± 0.024	0.495 ± 0.046
	24	0	0
	56	0.462 ± 0.023	0.420 ± 0.055
	26	0.425 ± 0.024	0.432 ± 0.020
	58	0.439 ± 0.023	0.408 ± 0.034

Table 3.3: Tractography analysis: mean and standard deviation of FA for each tract. The column on the right shows the values of difference in location calculated by the Wilcoxon Rank-Sum test

ROI index		**FA statistics**	
Seed	Target	Controls	SP MS patients
10	42	0.442 ± 0.033	0.407 ± 0.019
	21	0.426 ± 0.022	0.401 ± 0.021
	53	0	0
	23	0.449 ± 0.021	0.414 ± 0.038
	55	0	0
	24	0.318 ± 0.026	0.295 ± 0.035
	56	0.469 ± 0.034	0.431 ± 0.034
	26	0.394 ± 0.022	0.371 ± 0.025
	58	0.484 ± 0.031	0.446 ± 0.034
42	21	0	0
	53	0.447 ± 0.019	0.420 ± 0.026
	23	0	0
	55	0.461 ± 0.020	0.419 ± 0.040
	24	0.463 ± 0.030	0.434 ± 0.024
	56	0.302 ± 0.022	0.289 ± 0.025
	26	0.476 ± 0.023	0.441 ± 0.030
	58	0.403 ± 0.021	0.381 ± 0.030
21	53	0.473 ± 0.025	0.427 ± 0.048
	23	0.421 ± 0.025	0.387 ± 0.037
	55	0.418 ± 0.025	0.391 ± 0.035
	24	0.431 ± 0.027	0.412 ± 0.038
	56	0.426 ± 0.030	0.410 ± 0.045
	26	0.418 ± 0.023	0.388 ± 0.035
	58	0.465 ± 0.033	0.424 ± 0.045
53	23	0.426 ± 0.024	0.393 ± 0.031
	55	0.415 ± 0.024	0.382 ± 0.038
	24	0.421 ± 0.026	0.400 ± 0.060
	56	0.421 ± 0.030	0.400 ± 0.043
	26	0.454 ± 0.028	0.412 ± 0.048
	58	0.417 ± 0.024	0.387 ± 0.035
23	55	0.406 ± 0.022	0.357 ± 0.039
	24	0.431 ± 0.024	0.405 ± 0.034
	56	0.434 ± 0.025	0.406 ± 0.042
	26	0.451 ± 0.019	0.428 ± 0.020
	58	0.425 ± 0.022	0.395 ± 0.036
55	24	0.445 ± 0.023	0.417 ± 0.049
	56	0.425 ± 0.028	0.401 ± 0.038
	26	0.415 ± 0.023	0.387 ± 0.040
	58	0.463 ± 0.018	0.435 ± 0.024
24	56	0.466 ± 0.036	0.424 ± 0.072
	26	0.351 ± 0.034	0.336 ± 0.059
	58	0.413 ± 0.034	0.377 ± 0.057
56	26	0.446 ± 0.034	0.399 ± 0.069
	58	0.362 ± 0.033	0.334 ± 0.068
26	58	0.375 ± 0.026	0.345 ± 0.038

Tractography analysis: mean and standard deviation of FA for each tract

according to their loading over the first PN. From a visual inspection we observed that the values of FA in the patients' matrix were generally lower than the respective values in the controls' matrix.

Analysis of changes between the two groups

We analyzed the changes between the two groups with the same methods used in the study of GM. First, by applying increasing thresholds to the connectivity matrices, we checked the variability of Eg in the respective networks. Then we ran the Mann-Whitney U test with a global false positive rate of 0.05.
In the study of Eg variations we considered a range of thresholds less wide than in the GM. In fact, compared to the first PN, the network describing WM connectivity was smaller and became inconsistent if edge weights were thresholded with values higher than 0.4. For this reason in the resulting plot (Figure 3.6) we could still observe a decreasing trend, but not the final plateau of Figure 3.4. There was instead the same initial constant behaviour, although here the Eg had maximum value < 1 because the corresponding network was not fully-connected.
Finally, as a result of the Mann-Whitney U test, all the distributions of FA listed in Table 3.3 were found to be statistically different between the two groups. So, in this case, we could not identify a specific subset of features mainly responsible for the differentiation between healthy subjects and patients.

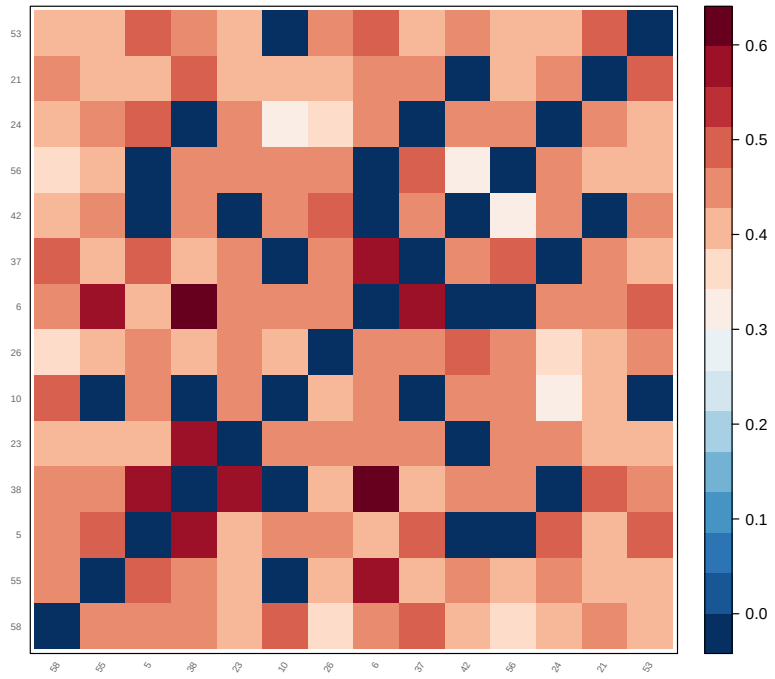

(a) Healthy controls

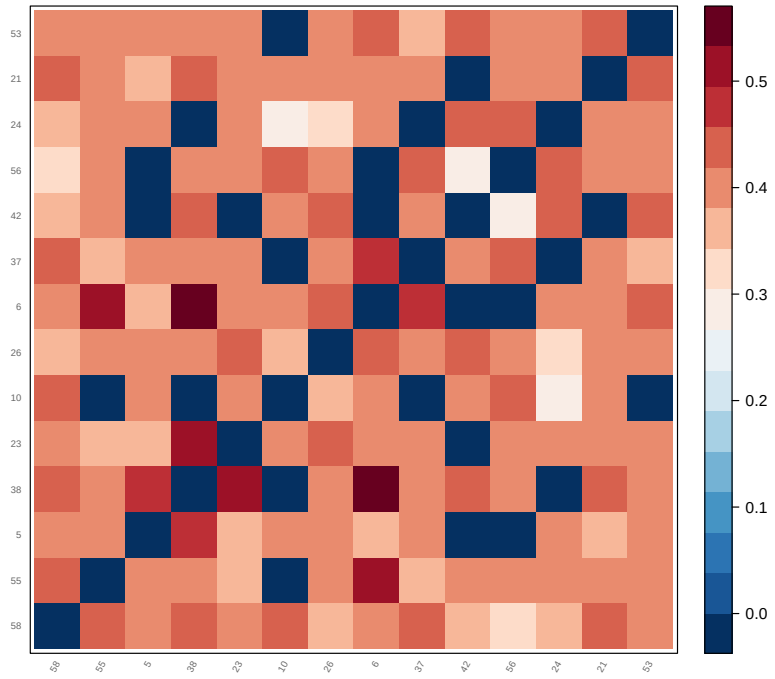

(b) SP MS patients

Figure 3.5: Connectivity matrices based on FA values: cortical regions are ordered according to their loadings over the first PN of healthy controls

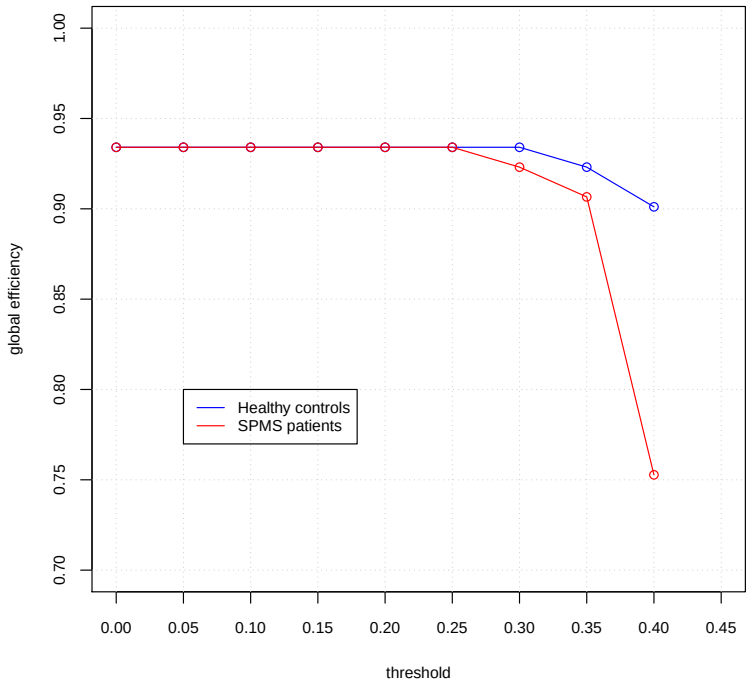

Figure 3.6: Global Efficiency of the WM connectivity matrices. The plot compares the Eg of the first PN sub-network for increasing values of threshold applied to the connectivity matrices

3.3 Relationship between GM and WM connectivity

To summarize, in our work we considered a group of healthy subjects and a group of patients suffering from SP MS. For each group we determined:

1. a network that describes connectivity between a set of cortical regions;
2. a network that describes connectivity of the underlying WM.

In the final part of our analysis we considered, only for the healthy controls, the set of connections between regions included in both the networks, i.e. the entire matrix of mean FA values in the WM, and the corresponding sub-matrix of correlation values in the GM. With R, we compared statistically the samples of correlation and FA values of each region, observing their empirical cumulative distribution functions and the Quantile-Quantile (QQ) plot. The empirical cumulative distribution function, called Fn in the R plots, is a step function with jumps i/n at observation values, where i is the number of tied observations at that value. Missing values are ignored. For observations $x = (x_1, x_2, ...x_n)$, $Fn(t)$ is the fraction of observations less or equal to t.
The Quantile-Quantile plot is a graphical technique for determining if two samples come from populations with a common distribution. The k-th q-quantile for a variable is the value z such as the probability for the variable to be less than z is at most k/q. With R, we plotted the quantiles of the first data set against the quantiles of the second data set. We also plotted a reference line: if the two samples come from a population with the same distribution, the points should fall approximately along this reference line. For two samples x and y we used the code written in Listing 4.5 in the Code listing appendix, where x was set equal to the distribution of correlations in the GM connectivity matrix, and y was the corresponding sample of mean FA of the WM tracts.
By observing the cumulative distribution functions and the QQ plots, we found that values of correlation and FA never came from the same distribution, for any of the considered cortical areas. As an example of the obtained results, in Figure 3.7 we show the graphs created for the left inferior parietal gyrus. In Figure 3.7a there were no overlaps of the two functions, and in Figure 3.7b the distribution of the quantiles was distant from the theoretical one. In conclusion, the two networks did not describe the same pattern of connectivity. We observed this result only in a subset of cortical regions, but we could reasonably think to extend the conclusion to all the areas considered in our work.

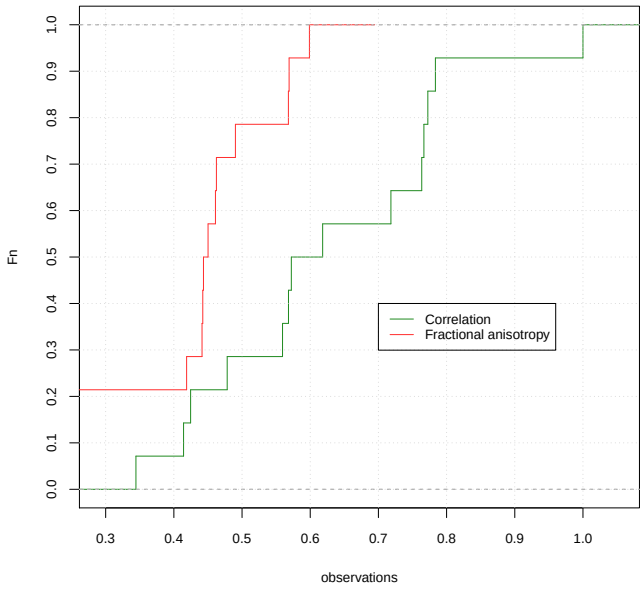

(a) Empirical cumulative distribution functions

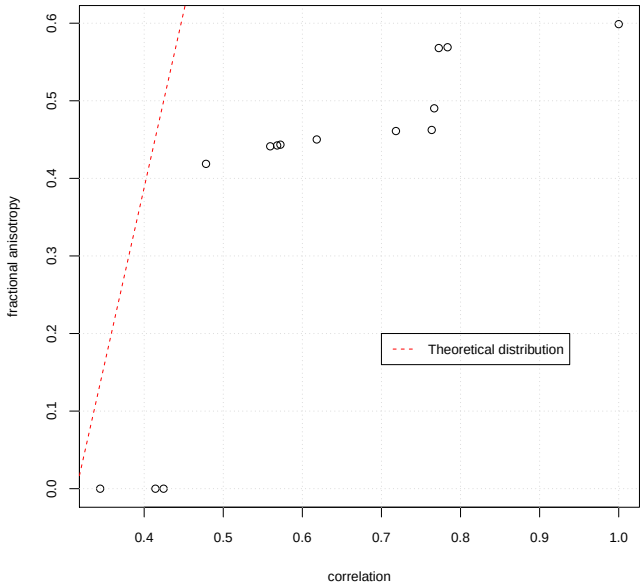

(b) QQ plot

Figure 3.7: Superior frontal gyrus: comparing GM and WM metrics of connectivity. The metrics are described by the distributions of correlation and FA values, respectively derived from the GM and WM connectivity matrices

Chapter 4

Conclusions

With the work described in this dissertation we developed a multi-modal analysis of brain anatomical connectivity using quantitative Magnetic Resonance Imaging data.
We used the Principal Networks technique on a T1-w data set of healthy controls to first determine the whole matrix describing brain connectivity and then its most influential sub-network, called first Principal Network. By analyzing the most connected regions of this sub-network, we observed a good reproducibility of the PNs technique, then, by using a leave-one-out approach, we cross-validated it within our data set. Given these results, we suggest the pipeline just described as a tool for calculating and validating the brain's main influential sub-network.
We compared the connectivity properties of the controls' first PN with the ones of the equivalent sub-network determined from data of Secondary-Progressive Multiple Sclerosis patients. We quantified the loss of topological properties by applying a set of thresholds to the edges weights of the two networks. As a result, the Global Efficiency of the first PN was systematically lower in the network of patients than in the network of controls. This suggested not only that cortical parameters are different between SP MS patients and healthy subjects, as demonstrated in [53], but also that this difference affects the efficiency of the main brain sub-network. By testing the statistical difference of cortical thickness data in the two groups, we identified the regions of GM mainly responsible for the changes in the two networks, and we observed that the result was not characterized by a strong hemispheric lateralization.
In order to investigate the relationship between patterns of connectivity in the GM and in the WM, we applied the tractography technique and determined the value of mean Fractional Anisotropy for each tract of interest. We analyzed connectivity between a specific subset of sub-cortical WM regions, which underlie the GM areas of the first PN. We determined a network describing connectivity in the WM for both the groups of subjects. By applying the same analysis used before, we found again a loss of Eg in the patients' network, although here the statistical comparison could not individuate a specific source for the differentiation of the two groups. In fact, as a result of the test, the distributions of FA values were different for each tract we considered.
A last important result was shown by the two patterns of connectivity determined from data of healthy controls. For this last study we focused on the interconnections between the regions previously analyzed with the tractography. For each region, we compared the two distributions of parameters weighting its connections in the two

networks. The distributions were respectively formed by the values of correlations calculated from cortical thickness parameters and the values of FA: the observation of their empirical cumulative distribution functions as well as the comparison of their quantiles revealed a different pattern of connectivity in the WM from that of the GM, confirming that WM structural connections and GM functional connections reveal information on complementary but independent systems.

At the end of this work, we can conclude that analysis of connectivity in the GM, based on correlation between cortical thickness values, should be held independently from the analysis of connectivity in the underlying WM. There is no evidence of correlation between the two metrics we adopted to quantify connectivity in the two structures of the brain. However, we found that SP MS affects the efficiency of brain connectivity in both the WM and the GM.

We must remember that the methods we applied have some limitations. In the first place, FreeSurfer's cortical reconstruction process has an accuracy of 0.5mm, while cortical thickness varies in the range of $[0.5, 4]$mm: this could lead to errors while measuring the cortical parameters, and, therefore, while determining the PNs. However, when we applied the PNs technique we obtained reproducible and reliable results, so we could be confident that our work was not affected consistently.

Another important limitation is given by the group nature of the PNs calculation: in fact, this method does not allow us to calculate the relevant sub-networks of the brain from data of a single subject, so what we obtain is always an average outcome influenced by the characteristics of all the subjects. However, this could be an advantage, since a mean result is more robust and less sensitive to possible outliers.

We should also consider the limitations of tractography, which has often difficulties in reconstructing the tracts in the presence of crossing fibres. Again, we could state that our results were reliable, since we used High Angular Resolution Diffusion Imaging to resolve multiple fibres orientations and a software, MRtrix, accounting for fibre crossing.

Several future developments are possible for this work. The same approach could be used to compare loss of efficiency in patients affected by other kind of MS, and possibly to investigate the progression of the disease. Moreover, other DT-derived metrics, such as the Mean Diffusivity (MD), could be quantified and analyzed in conjunction with the FA.

Finally, it could be interesting to develop a clinical application of these findings. For this purpose it would be essential a collaboration between people with different cultural backgrounds, in order to get new insight about the nature and progression of MS.

Acknowledgements

In this section there are all those people I wish to acknowledge for this work.

Claudia Wheeler-Kingshott, Matteo Pardini and the Nuclear Magnetic Resonance Research Unit of the UCL Institute of Neurology.

Jonathan D. Clayden and Jamie Kawadler of the UCL Institute of Child Health for the help with TractoR and FreeSurfer.

Fulvia Palesi of the University of Pavia for her precious assistance with MRtrix.

Vanessa Lippolis for the introduction to her Master's thesis results, on which my work was partially based.

Code listing

In this appendix we report the code used to perform the analyses of this work. The two bash scripts in Listing 4.1 and Listing 4.2 were originally written by Fulvia Palesi. The R scripts in Listing 4.3 and Listing 4.5 and the R function in Listing 4.4 were written by the author of the thesis.

```
#!/bin/bash

if [[ $# -lt 3 ]] ; then
  echo "Incorrect Number of Paramaters Specified"
  echo "Usage: <original bvecs> <rotated bvecs> <ecclog> [-k]"
  echo ""
  echo "<ecclog> the output log file from ecc"
  echo "-k keep the mat files"
  echo ""
  exit 1;
fi

ECCLOG=$3;
LIST="mat.list"

if [ ! -e $1 ] ; then
  echo "Source bvecs $1 does not exist!"
  exit 1
fi


if [ -e $2 ] ; then
  echo "Target bvecs: $2 already exists!"
  exit 1
fi

if [ ! -e $ECCLOG ]; then
  echo "Ecc log file $3 does not exist!"
  exit 1
fi

if [ "$4" == "-k" ] ; then
  KEEP="YES"
else
  KEEP="NO"
fi

######################################################################
# Create the mat files from input
#
# Here we read input ecclog file line by line, produce the FSL mat
# file and fill it with respective trasformation. File listing all
# the mat files generates is also created

if [ -e ${LIST} ]
then
  rm ${LIST}
fi

cat ${ECCLOG} | while read line; do
    #create a file name from processed volumes
    matfile=$(remove_ext $(echo ${line} | grep processing | gawk '{print $2}'));
    if [ "${matfile}" != "" ] ; then
```

```
     matfile=${matfile}.mat;
       echo "Generating ... ${matfile}";
       echo ${matfile} >> ${LIST};
       # following two reads will deal with unimportant lines
       read line;
       read line;
       # read matrix and store it in the current matfile
       read line;
       echo ${line} > ${matfile};
       read line;
       echo ${line} >> ${matfile};
       read line;
       echo ${line} >> ${matfile};
       read line;
       echo ${line} >> ${matfile};
    fi
 done
#
##############################################################################

##############################################################################
# rotate bvecs

newXs="";
newYs="";
newZs=""


BVECS=$1;
Xs=$(cat $BVECS | head -1 | tail -1)
Ys=$(cat $BVECS | head -2 | tail -1)
Zs=$(cat $BVECS | head -3 | tail -1)

MATs=$(cat mat.list);

VOLUMES=$(cat $BVECS | head -1 | tail -1 | wc -w)

if [ $VOLUMES != $(echo ${MATs} | wc -w) ]
then
  echo "Number of *.mat files in $3 is not equal to number"
  echo "of gradients in $BVECS!"
  exit 1
fi

i=1
while [ $i -le $VOLUMES ] ; do
  MAT=$(echo ${MATs} | cut -d " " -f ${i});
  #echo $MAT

  output=$(avscale --allparams ${MAT} | head -2 | tail -1)
  m11=$(echo $output | cut -d " " -f 1)
  m12=$(echo $output | cut -d " " -f 2)
  m13=$(echo $output | cut -d " " -f 3)
  m11=$(printf "%1.7f" $m11)
  m12=$(printf "%1.7f" $m12)
  m13=$(printf "%1.7f" $m13)

  output=$(avscale --allparams ${MAT} | head -3 | tail -1)
  m21=$(echo $output | cut -d " " -f 1)
  m22=$(echo $output | cut -d " " -f 2)
  m23=$(echo $output | cut -d " " -f 3)
  m21=$(printf "%1.7f" $m21)
  m22=$(printf "%1.7f" $m22)
  m23=$(printf "%1.7f" $m23)

  output=$(avscale --allparams ${MAT} | head -4 | tail -1)
  m31=$(echo $output | cut -d " " -f 1)
  m32=$(echo $output | cut -d " " -f 2)
  m33=$(echo $output | cut -d " " -f 3)
  m31=$(printf "%1.7f" $m31)
  m32=$(printf "%1.7f" $m32)
  m33=$(printf "%1.7f" $m33)
```

```
  X=$(echo $Xs | cut -d " " -f "$i")
  Y=$(echo $Ys | cut -d " " -f "$i")
  Z=$(echo $Zs | cut -d " " -f "$i")
  X=$(printf "%1.7f" $X)
  Y=$(printf "%1.7f" $Y)
  Z=$(printf "%1.7f" $Z)

  rX=$(echo "scale=7;  ($m11 * $X) + ($m12 * $Y) + ($m13 * $Z)" | bc -l);
  rY=$(echo "scale=7;  ($m21 * $X) + ($m22 * $Y) + ($m23 * $Z)" | bc -l);
  rZ=$(echo "scale=7;  ($m31 * $X) + ($m32 * $Y) + ($m33 * $Z)" | bc -l);

  rX=$(printf "%1.7f" $rX)
  rY=$(printf "%1.7f" $rY)
  rZ=$(printf "%1.7f" $rZ)

# echo $rX" "$rY" "$rZ;

  rXs=${rXs}${rX}" ";
  rYs=${rYs}${rY}" ";
  rZs=${rZs}${rZ}" ";

  i=$(echo "$i + 1" | bc) ;
done

echo "$rXs" >> $2;
echo "$rYs" >> $2;
echo "$rZs" >> $2;
#
######################################################################

if [ "$KEEP" == "NO" ]; then
  rm $MATs $LIST
fi
```

Listing 4.1: 01_rotbvecs

```
#!/bin/bash

   #Translation of each subject's brain in a common space
   echo "Registration of all DTI images in a common space"
   flirt -in nodif_brain -ref /data/mrtrix/template -out nodif_brain_mni -omat
       nodif.mat -bins 256 -cost corratio -searchrx -90 90 -searchry -90 90 -
       searchrz -90 90 -dof 6 -schedule /usr2/mrtools/fsl/live/etc/flirtsch/
       sch3Dtrans_3dof -interp nearestneighbour
   for file in vol*.nii.gz
   do
      flirt -in $file -ref /data/mrtrix/template.nii -o $file -applyxfm -init nodif
          .mat -interp nearestneighbour
   done
   fslmerge -t data_b0.nii vol*
   mv vol0000.nii.gz b0.nii.gz
   echo "Brain Extraction on b0 image in a common space"
   bet b0 b0_brain -f 0.3 -g 0 -m
   rm -f vol*

   #Translation of T13D image onto DTI image in a common space
   echo "Brain Extraction on T13D image"
   bet T13D T13D_brain -B -f 0.3 -g 0
   rm -f T13D_brain_mask.nii.gz
   echo "Registration from T13D space into DTI common space"
   flirt -in b0_brain -ref T13D_brain -out b0onT13D -omat b0onT13D.mat -bins 256 -
       cost normmi -searchrx -90 90 -searchry -90 90 -searchrz -90 90 -dof 6 -
       interp nearestneighbour
   convert_xfm -omat T13Donb0.mat -inverse b0onT13D.mat
   flirt -in T13D -applyxfm -init T13Donb0.mat -out T13Donb0 -paddingsize 0.0 -
       interp nearestneighbour -ref b0_brain
```

Listing 4.2: 02_common_space

```
1 # Main script
2
3 # Required packages
```

```
4  library(tractor.base)
5  library(tractor.graph)
6  library(tractor.session)
7  library(reportr)
8  library(lattice)
9
10
11 # Healthy controls ------------------------------------------------------
12
13 # Creation of a list of sessions
14 controls.list   <- read.table("list-of-controls.txt", header = TRUE, sep = "")
15 controls.number <- length(controls.list$Controls)
16 controls.sessionList <- list()
17 for (i in (1:controls.number)) {
18   currentPath <- paste("/data/erasmus13/subjects/", controls.list$Controls[i],
19                        sep = "")
20   controls.sessionList[[i]] <- newSessionFromDirectory(currentPath)
21 }
22
23 # Cortical thickness data matrix
24 controls.dataMatrix <-
25   createCorticalThicknessTableForSessions(controls.sessionList)
26 controls.scaledDataMatrix <-
27   matrixNormalization(controls.dataMatrix) # normalization
28
29 # Principal graphs calculation
30 controls.graph <- newGraphFromTable(controls.scaledDataMatrix, "correlation")
31 controls.principalGraphs <-
32   calculatePrincipalGraphsForGraphs(controls.graph, loadingThreshold = 0.1)
33
34 # First Principal Network full association matrix
35 controls.PN1connectionMatrix <-
36   controls.principalGraphs$componentGraphs$PN1$getConnectionMatrix()
37 pg <- lapply(controls.principalGraphs$componentGraphs,
38              newGraphWithEdgeWeightThreshold, threshold = 0.2, ignoreSign = TRUE)
39
40 # First PN graph plot
41 plot(pg[[1]], col = 4, cex = 0.7, weightLimits = c(-1,1),
42      ignoreBeyondLimits = FALSE, useAlpha = FALSE, hideDisconnected = TRUE,
43      order = order(controls.principalGraphs$eigenvectors[,1]),
44      title("Controls: 1st Principal Network"))
45
46 # Full association matrix lattice plot
47 levelplot.Graph(controls.graph, cex = 0.7,
48                 main = "Controls: full association matrix derived from all cortical
                        thickness data",
49                 sub = "gyral regions ordered by index")
50
51 # Ordered full association matrix lattice plot
52 png("controls.orderedFullMatrix.pdf")
53 levelplot.Graph(controls.graph, cex = 0.7,
54                 order = order(controls.principalGraphs$eigenvectors[,1]),
55                 main = "Controls: full association matrix derived from all cortical
                        thickness data",
56                 sub = "gyral regions ordered by their loadings in the first
                       principal network")
57
58
59 # Results validation: leave-one-out -------------------------------------
60
61 # initializating empty data structures
62 controls.leaveOneOut.correlationMatrices <-
63   array(NA, dim = c((controls.number - 1), 64, controls.number))
64 controls.leaveOneOut.principalGraphs <- list()
65 controls.leaveOneOut.PN1connectionMatrices <-
66   array(NA, dim = c(64, 64, controls.number))
67
68 # PNs calculation for 32 groups of 31 subjects
69 for (i in (1:controls.number)) {
70   if ((i == 1) || (i == controls.number)) {
71     if (i == 1) {
72       matrix <- createCorticalThicknessTableForSessions(
73         controls.sessionList[2:controls.number])
```

```
    }
    if (i == controls.number) {
      matrix <- createCorticalThicknessTableForSessions(
        controls.sessionList[1:(controls.number - 1)])
    }
  } else {
    setOfSessions <- union(controls.sessionList[1 : (i - 1)],
                           controls.sessionList[(i + 1):controls.number])
    matrix <- createCorticalThicknessTableForSessions(setOfSessions)
  }
  controls.leaveOneOut.correlationMatrices[, , i] <- matrix
  scaledMatrix <- matrixNormalization(matrix)
  graph <- newGraphFromTable(scaledMatrix)
  principalGraphs <-
    calculatePrincipalGraphsForGraphs(graph, loadingThreshold = 0.1)
  controls.leaveOneOut.principalGraphs[[i]] <- principalGraphs
  controls.leaveOneOut.PN1connectionMatrices[, , i] <-
    principalGraphs$componentGraphs$PN1$getConnectionMatrix()
}

# probOfConnection: each element is the probability that the corresponding
# element in the association matrix is not null
# connectionMean: reports the mean connection values between each pair of
# cortical regions
probabilityOfConnection <- matrix(nrow = 64, ncol = 64)
connectionMean <- matrix(nrow = 64, ncol = 64)
for (r in (1:64)) {
  for (c in (1:64)) {
    currentElement <- c()
    for (i in (1:controls.number)) {
      currentElement <- c(currentElement,
                          controls.leaveOneOut.PN1connectionMatrices[r, c, i])
    }
    missingConnections <- sum(currentElement == 0)
    probabilityOfConnection[r, c] <- ((32 - missingConnections) / 32)
    connectionMean[r, c] <- mean(currentElement)
  }
}

# differenceOfValues: each element reports the absolute difference value between
# the value of the connection matrix determined from all the subjects and the
# mean connection value of the leave one out analysis
differenceOfValues <- abs(controls.PN1connectionMatrix - connectionMean)

# Lattice plots settings
col <- tractor.base:::getColourScale(4)$colours
order = order(controls.principalGraphs$eigenvectors[,1])

# probabilityOfConnection lattice plot
rownames(probabilityOfConnection) <- seq(1,64)
colnames(probabilityOfConnection) <- seq(1,64)
levelplot(probabilityOfConnection[order, order],
          col.regions=col, useRaster = TRUE,
          scales=list(x=list(rot=60, col="grey40", cex = 0.5),
                      y=list(col="grey40", cex = 0.5)),
          xlab="", ylab="")
          main = paste("Probability of connection (min = ",
                       min(probabilityOfConnection), ", max = ",
                       max(probabilityOfConnection), ")", sep = ""),
          sub = "gyral regions ordered by their loadings in the first principal
              network")

# differenceOfValues lattice plot
rownames(differenceOfValues) <- seq(1,64)
colnames(differenceOfValues) <- seq(1,64)
levelplot(differenceOfValues[order, order], col.regions=col, useRaster = TRUE,
          scales=list(x=list(rot=60, col="grey40", cex = 0.5),
                      y=list(col="grey40", cex = 0.5)),
          xlab = "", ylab = "")
          main = paste("Difference with reference values (min = ",
                       min(differenceOfValues), ", max = ",
                       max(differenceOfValues), ")", sep = ""),
```

```
145           sub = "gyral regions ordered by their loadings in the first principal
                  network")
146
147
148 # SP patients ------------------------------------------------------------
149
150 ## Creation of a list of sessions
151 SPpatients.list   <-
152   read.table("list-of-SP-patients.txt", header = TRUE, sep = "")
153 SPpatients.number <- length(SPpatients.list$SPpatients)
154 SPpatients.sessionList <- list()
155 for (i in (1:SPpatients.number)) {
156   SPpatients.sessionList[[i]] <- newSessionFromDirectory(
157     paste("/data/erasmus13/subjects/", SPpatients.list$SPpatients[i], sep = ""))
158 }
159
160 # Cortical thickness data matrix
161 SPpatients.dataMatrix <-
162   createCorticalThicknessTableForSessions(SPpatients.sessionList)
163 SPpatients.scaledDataMatrix <-
164   matrixNormalization(SPpatients.dataMatrix) # normalization
165
166 # Correlation matrix
167 SPpatients.correlationMatrix <- cor(SPpatients.scaledDataMatrix)
168 allVerticesNames <- as.character(seq(1,64))
169 rownames(SPpatients.correlationMatrix) <- allVerticesNames
170 colnames(SPpatients.correlationMatrix) <- allVerticesNames
171
172 # Lattice plot settings
173 col <- tractor.base:::getColourScale(4)$colours
174 order = order(controls.principalGraphs$eigenvectors[,1])
175
176 # Ordered full association matrix lattice plot
177 SPpatients.orderedCorrelationMatrix <- SPpatients.correlationMatrix[order, order]
178 levelplot(SPpatients.correlationMatrix[order, order],
179           col.regions=col, useRaster = TRUE,
180           scales=list(x=list(rot=60, col="grey40", cex = 0.5, tck=0),
181                       y=list(col="grey40", cex = 0.5, tck=0)),
182           xlab = "", ylab = "",
183           main = "SP patients: full association matrix",
184           sub = "gyral regions ordered by their loadings in the controls' 1st PN")
```

Listing 4.3: mainScript.R

```
 1 matrixNormalization <- function(dataMatrix) {
 2   # Normalizes a cortical thickness matrix to have zero mean and unit standard
 3   # deviation in each cortical region across the subjects.
 4   # Arg:
 5   #   dataMatrix: the matrix to be normalized.
 6   # Return:
 7   #   normDataMatrix: the normalized matrix.
 8
 9   # Input matrix dimensions
10   size <- dim(dataMatrix)
11   nR <- size[1]
12   nC <- size[2]
13
14   dataMatrix.mean <- apply(dataMatrix, 2, mean)  # mean values by column
15   dataMatrix.sd   <- apply(dataMatrix, 2, sd)  # std deviation values by column
16
17   # Empty output matrix
18   normDataMatrix <- matrix(nrow = nR, ncol = nC)
19   if (!is.null(rownames(dataMatrix)))
20     rownames(normDataMatrix) <- rownames(dataMatrix)
21   if (!is.null(colnames(dataMatrix)))
22     colnames(normDataMatrix) <- colnames(dataMatrix)
23
24   # Values normalization
25   for (j in (1:nC)) {
26     m <- dataMatrix.mean[j]
27     stdev <- dataMatrix.sd[j]
28     for (i in (1:nR)) {
29       normDataMatrix[i, j] <- (dataMatrix[i, j] - m) / stdev
```

```
30     }
31   }
32
33   return(normDataMatrix)
34 }
```

Listing 4.4: matrixNormalization.R

```
1 # Tests if two samples x and y come from the same distribution
2 # by comparing their quantiles
3
4 qqplot(x, y)
5 aaa <- quantile(x, c(0.25, 0.75))
6 bbb <- quantile(y, c(0.25, 0.75))
7 coeff <- (aaa[2] - aaa[1]) / (bbb[2] - bbb[1])
8 inter <- aaa[1] - coeff * bbb[1]
9 abline(inter, coeff)
```

Listing 4.5: testQuantiles.R

Bibliography

[1] J. D. Clayden, M. Dayan, and C. A. Clark, "Principal networks," *PLoS ONE*, vol. 8(4), 2013.

[2] M. E. Haacke, R. W. Brown, M. R. Thompson, and R. Venkatesan, *Magnetic Resonance Imaging: Physical Principles and Sequence Design.* John Wiley & Sons., Inc., pp. 1-13, 24, 70, 71, 1999.

[3] J. P. Hornak, "The Basics of MRI." `http://www.cis.rit.edu/htbooks/mri/`. Accessed: 28th of May, 2014.

[4] D. K. Jones, K. T. R., and T. R., "White matter integrity, fiber count, and other fallacies: The do's and don'ts of diffusion MRI," *NeuroImage*, vol. 73, pp. 239–254, 2013.

[5] D. Denis Le Bihan, C. Poupon, A. Amadon, and F. Lethimonnier, "Artifacts and Pitfalls in Diffusion MRI," *Journal of Magnetic Resonance Imaging*, vol. 24, pp. 478–488, 2006.

[6] M. Patestas and L. P. Gartner, *A textbook of neuroanatomy.* Wiley-Blackwell, pp. 68-70, 75-77, 80, May 2006.

[7] O. Sporns, "Brain connectivity," *Scholarpedia*, vol. 2, no. 10, p. 4695, 2007. revision 91083.

[8] A. Griffa, P. S. Baumann, J.-P. Thiran, and P. Hagmann, "Structural connectomics in brain disease," *NeuroImage*, vol. 80, p. 515, 2013.

[9] "National multiple sclerosis society." `http://www.nationalmssociety.org/`. Accessed: 26th of May, 2014.

[10] Z. J. Chen, Y. He, P. Rosa-Neto, J. Germann, and A. C. Evans, "Revealing Modular Architecture of Human Brain Structural Networks by Using Cortical Thickness from MRI," *Cerebral Cortex*, vol. 18, pp. 2374–2381, October 2008.

[11] J. L. R. Rubenstein and P. Rakic, "Genetic Control of Cortical Development," *Cerebral Cortex*, vol. 9(6), pp. 521–523, 1999.

[12] B. Fischl, A. van der Kouwe, . Destrieux, C, E. Halgren, F. Segonne, D. H. Salat, E. Busa, L. J. Seidman, J. Goldstein, D. Kennedy, V. Caviness, . Makris, N, B. Rosen, and A. M. Dale, "Automatically Parcellating the Human Cerebral Cortex," *Cerebral Cortex*, vol. 14, pp. 11–22, 2004.

[13] B. Fischl and A. M. Dale, "Measuring the thickness of the human cerebral cortex from magnetic resonance images," *Proceedings of the National Academy of Sciences*, vol. 97, pp. 11044–11049, 2000.

[14] M. Reuter, "FreeSurfer Analysis Pipeline Overview." `http://surfer.nmr.mgh.harvard.edu/fswiki/FreeSurferAnalysisPipelineOverview`, April 2011. Accessed: 30th of April, 2014.

[15] A. M. Dale, B. Fischl, and M. I. Sereno, "Cortical surface-based analysis i: Segmentation and surface reconstruction," *NeuroImage*, vol. 9(2), pp. 179–194, 1999.

[16] B. Fischl, M. Sereno, and A. M. Dale, "Cortical surface-based analysis ii: Inflation, flattening, and surface-based coordinate system," *NeuroImage*, vol. 9(2), pp. 195–207, 1999.

[17] F. Segonne, A. Dale, E. Busa, M. Glessner, U. Salvolini, H. Hahn, and B. Fischl, "A Hybrid Approach to the Skull-Stripping Problem in MRI," *NeuroImage*, vol. 22(3), pp. 1060–1075, 2004.

[18] B. Fischl, M. Sereno, R. Tootell, and A. Dale, "High-resolution inter-subject averaging and a coordinate system for the cortical surface," *Human Brain Mapping*, vol. 8(4), pp. 272–284, 1999.

[19] B. Fischl, D. Salat, E. Busa, M. Albert, M. Dieterich, C. Haselgrove, A. van der Kouwe, R. Killiany, D. Kennedy, S. Klaveness, A. Montillo, N. Makris, B. Rosen, and A. Dale, "Whole brain segmentation: Automated labeling of neuroanatomical structures in the human brain," *Neuron*, vol. 33(3), pp. 341–355, January 2002.

[20] B. Fischl, D. Salat, A. van der Kouwe, N. Makris, F. Segonne, B. Quinn, and A. Dale, "Sequence-Independent Segmentation of Magnetic Resonance Images," *NeuroImage*, vol. 23, pp. S69–S84, 2004.

[21] R. S. Desikan, F. SÃ©gonne, B. Fischl, B. T. Quinn, B. C. Dickerson, D. Blacker, A. M. Buckner, Randy L.and Dale, R. P. Maguire, B. T. Hyman, M. S. Albert, and R. J. Killiany, "An automated labeling system for subdividing the human cerebral cortex on MRI scans into gyral based regions of interest," *NeuroImage*, vol. 31, pp. 968–980, 2006.

[22] R. Preciado, "Making Edits to the White Matter." `http://surfer.nmr.mgh.harvard.edu/fswiki/FsTutorial/WhiteMatterEdits_freeview`, April 2014. Accessed: 30th of April, 2014.

[23] M. Ebling, "Using Control Points to Fix Intensity Normalization." `http://surfer.nmr.mgh.harvard.edu/fswiki/FsTutorial/ControlPoints_freeview`, November 2013. Accessed: 30th of April, 2014.

[24] J. D. Clayden, S. Muñoz Maniega, A. J. Storkey, M. D. King, M. E. Bastin, and C. A. Clark, "TractoR: Magnetic resonance imaging and tractography with R," *Journal of Statistical Software*, vol. 44, pp. 1–18, 2011.

[25] R Core Team, *R: A Language and Environment for Statistical Computing*. R Foundation for Statistical Computing, Vienna, Austria, 2013. `http://www.R-project.org`.

[26] M. Jenkinson, C. F. Beckmann, T. E. Behrens, M. W. Woolrich, and S. M. Smith, "FSL," *NeuroImage*, vol. 62, pp. 782–790, 2012.

[27] M. W. Woolrich, S. Jbabdi, B. Patenaude, M. Chappell, S. Makni, T. Behrens, C. Beckmann, M. Jenkinson, and S. M. Smith, "Bayesian analysis of neuroimaging data in FSL," *NeuroImage*, vol. 45, pp. S173–86, 2009.

[28] S. M. Smith, M. Jenkinson, M. W. Woolrich, C. Beckmann, T. E. J. Behrens, H. Johansen-Berg, P. Bannister, M. De Luca, I. Drobnjak, R. Niazy, J. Sanuders, J. Vickers, Y. Zhang, N. De Stefano, J. M. Brady, and P. M. Matthews, "Advances in functional and structural MR image analysis and implementation as FSL," *NeuroImage*, vol. 23(S1), pp. 208–219, 2004.

[29] The MathWorks Inc., Natick, Massachusetts, *MATLAB version R2013a (8.1.0.604)*, February 2013. `www.mathworks.co.uk/products/matlab`.

[30] J.-D. Tournier, *MRtrix version 0.2.11*. Brain Research Institute, Melbourne, Australia, 2012. `http://www.brain.org.au/software/mrtrix/index.html`.

[31] J.-D. Tournier, F. Calamante, and A. Connelly, "MRtrix: Diffusion Tractography in Crossing Fibers Regions," *International Journal of Imaging Systems and Technology*, vol. 22(1), pp. 53–66, March 2012.

[32] UCL Computer Science, *NiftyReg*. `www0.cs.ucl.ac.uk/staff/M.Modat/Marcs_Page/Software.html`.

[33] S. Ourselin, R. Stefanescu, and X. Pennec, "Robust registration for multi-modal images: Towards real-time clinical applications," *MICCAI*, 2002.

[34] S. Ourselin, A. Roche, G. Subsol, X. Pennec, and N. Ayache, "Reconstructing a 3D structure from serial histological sections," *Image and Vision Computing*, vol. 19(1-2), pp. 25–31, 2001.

[35] M. Modat, G. R. Ridgway, Z. A. Taylor, M. Lehmann, J. Barnes, N. C. Fox, D. J. Hawkes, and S. Ourselin, "Fast free-form deformation using graphic processing units," *Comput. Methods Programs Bioned.*, vol. 98(3), pp. 278–84, 2009.

[36] S. M. Smith, "Fast robust automated brain extraction," *Human Brain Mapping*, vol. 17(3), pp. 143–155, November 2002.

[37] M. Jenkinson, P. Bannister, M. Brady, and S. Smith, "Improved Optimization for the Robust and Accurate Linear Registration and Motion Correction of Brain Images," *NeuroImage*, vol. 17, pp. 825–841, 2002.

[38] M. Jenkinson and S. M. Smith, "A global optimisation method for robust affine registration of brain images," *Medical Image Analysis*, vol. 5(2), pp. 143–156, 2001.

[39] P. J. Basser and D. K. Jones, "Diffusion-tensor MRI: theory, experimental design and data analysis - a technical review," *NMR in Biomedicine*, vol. 15, pp. 456–467, 2002.

[40] N. Muhlert, V. Sethi, T. Schneider, P. Daga, L. Cipolotti, A. Haroon, Hamied, G. J. M. Parker, S. Ourselin, C. A. M. Wheeler-Kingshott, D. H. Miller, M. A. Ron, and D. Chard, "Diffusion MRI-Based Cortical Complexity Alterations Associated With Executive Function in Multiple Sclerosis," *Journal of magnetic resonance imaging*, vol. 38, pp. 54–63, 2013.

[41] M. Reuter, "How to Convert from FreeSurfer Space Back to Native Anatomical Space." `http://surfer.nmr.mgh.harvard.edu/fswiki/FsAnat-to-NativeAnat`, January 2014. Accessed: 26th of April, 2014.

[42] M. Jenkinson, "Orientation explained." `http://fsl.fmrib.ox.ac.uk/fsl/fslwiki/Orientation%20Explained`, November 2013. Accessed: 05th of May, 2014.

[43] J.-D. Tournier, F. Calamante, D. G. Gadian, and A. Connelly, "Direct estimation of the fiber orientation density function from diffusion-weighted MRI data using spherical deconvolution," *NeuroImage*, vol. 23(3), pp. 1176–1185, 2004.

[44] J.-D. Tournier, F. Calamante, and A. Connelly, "Robust determination of the fibre orientation distribution in diffusion mri: non-negativity constrained super-resolved spherical deconvolution," *NeuroImage*, vol. 35(4), pp. 1459–1472, 2007.

[45] J.-D. Tournier, "Data pre-processing." `http://www.brain.org.au/software/mrtrix/tractography/preprocess.html`, December 2011. Accessed: 27th of April, 2014.

[46] J. Mazziotta, A. Toga, A. Evans, P. Fox, and J. Lancaster, "A probabilistic atlas of the human brain: theory and rationale for its development," *NeuroImage*, vol. 2, pp. 89–101, 1995.

[47] J. Mazziotta, A. Toga, A. Evans, P. Fox, J. Lancaster, K. Zilles, R. Woods, T. Paus, G. Simpson, B. Pike, C. Holmes, D. Collins, P. Thompson, D. MacDonald, M. Iacoboni, T. Schormann, K. Amunts, N. Palomero-Gallagher, S. Geyer, L. Parsons, K. Narr, N. Kabani, G. LeGoualher, D. Boomsma, T. Cannon, R. Kawashima, and B. Mazoyer, "A probabilistic atlas and reference system for the human brain: International Consortium for Brain Mapping (ICBM)," *Philos. Trans. R. Soc. London B Biol. Sci.*, vol. 356, pp. 1293–1322, 2001.

[48] J. Mazziotta, A. Toga, A. Evans, P. Fox, J. Lancaster, K. Zilles, R. Woods, T. Paus, G. Simpson, B. Pike, C. Holmes, D. Collins, P. Thompson, D. MacDonald, M. Iacoboni, T. Schormann, K. Amunts, N. Palomero-Gallagher, S. Geyer, L. Parson, K. Narr, N. Kabani, G. LeGoualher, D. Boomsma, T. Cannon, R. Kawashima, B. Mazoyer, and I. C. for Brain Mapping, "Four-dimensional probabilistic atlas of the human brain," *J. Am. Med. Inform. Assoc. (JAMIA)*, vol. 8 (5), pp. 401–430, 2001.

[49] M. Pardini, F. G. Garacic, L. Bonzano, L. Roccatagliata, M. G. Palmieri, E. Pompili, F. Coniglione, F. Krueger, A. Ludovici, R. Floris, F. Benassi, , and L. Emberti Gialloreti, "White matter reduced streamline coherence in young men with autism and mental retardation," *European Journal of Neurology*, vol. 16, pp. 1185–1190, 2009.

[50] S. E. Leh, H. Johansen-Berg, and A. Ptito, "Unconscious vision: new insights into the neuronal correlate of blindsight using diffusion tractography," *Brain*, vol. 129, pp. 1822–1832, 2006.

[51] D. S. Tuch, T. G. Reese, M. R. Wiegell, N. Makris, J. W. Belliveau, and V. J. Wedeen, "High Angular Resolution Diffusion Imaging Reveals Intravoxel White Matter Fiber Heterogeneity," *Magnetic Resonance in Medicine*, vol. 48, pp. 577–582, 2002.

[52] P. van der Meulen, J. P. Groen, A. M. C. Tinus, and G. Bruntink, "Fast Field Echo imaging: an overview and contrast calculations," *Magnetic Resonance Imaging*, vol. 6, pp. 355–368, 1988.

[53] V. Lippolis, "Modelization by regression of cortical and cognitive parameters in healthy subjects and Multiple Sclerosis patients," diploma thesis, University of Pavia, 2013.

[54] L. Soliani, "Manuale di statistica per la ricerca e la professione – Metodi non parametrici per due campioni indipendenti." `http://www.dsa.unipr.it/soliani/capu9.pdf`, April 2005. Accessed: 12th of June, 2014.